minerals

MDPI

Article

Petrogenesis and Tectonic Significance of the ~276 Ma Baixintan Ni-Cu Ore-Bearing Mafic-Ultramafic Intrusion in the Eastern Tianshan Orogenic Belt, NW China

Minxin You [1,2], Wenyuan Li [2,*], Houmin Li [1,*], Zhaowei Zhang [2] and Xin Li [3]

[1] Key Laboratory of Metallogency and Mineral Resource Assessment, MNR, Institute of Mineral Resources, CAGS, Beijing 100037, China; youminxin_cgs@163.com
[2] Key Laboratory for the Study of Focused Magmatism and Giant Ore Deposit, MNR, Xi'an Center of Geological Survey, CGS, Xi'an 710054, China; zhaoweiz@126.com
[3] No. 1 Regional Geological Survey Party of Xinjiang Geology and Mineral Development Center, Urumqi 830011, China; donkey0000@163.com
* Correspondence: xalwenyuan@126.com (W.L.); lihoumin2002@163.com (H.L.)

Abstract: The Baixintan mafic-ultramafic intrusion in the Dananhu-Tousuquan arc of the Eastern Tianshan orogenic belt is composed of lherzolite, olivine gabbro, and gabbro. Olivine gabbros contain zircon grains with a U-Pb age of 276.8 ± 1.1 Ma, similar to the ages of other Early Permian Ni-Cu ore-bearing intrusions in the region. The alkaline-silica diagrams, AFM diagram, together with the Ni/Cu-Pd/Ir diagram, indicate that the parental magmas for the Baixintan intrusion were likely high-Mg tholeiitic basaltic in composition. The Cu/Pd ratios, the relatively depleted PGEs and the correlations between them demonstrate that the parental magmas had already experienced sulfide segregation. The lower CaO content in pyroxenites compared with the Duke Island Alaskan-type intrusion and the composition of spinels imply that Baixintan is not an Alaskan-type intrusion. By comparing the Baixintan intrusion with other specific mafic-ultramafic intrusions, this paper considers that the mantle source of the Baixintan intrusion is metasomatized by subduction slab-derived fluids' components, which gives rise to the negative anomalies of Nb, Ti, and Ta elements. Nb/Yb-Th/Yb, Nb/Yb-TiO_2/Yb, and Th_N-Nb_N plots show that the Baixintan intrusion was emplaced in a back-arc spreading environment and may be related to a mantle plume.

Keywords: Eastern Tianshan; Baixintan; Ni-Cu ore-bearing mafic-ultramafic intrusions; Early Permian; tectonic setting

Citation: You, M.; Li, W.; Li, H.; Zhang, Z.; Li, X. Petrogenesis and Tectonic Significance of the ~276 Ma Baixintan Ni-Cu Ore-Bearing Mafic-Ultramafic Intrusion in the Eastern Tianshan Orogenic Belt, NW China. *Minerals* **2021**, *11*, 348. https://doi.org/10.3390/min11040348

Academic Editor: Andrei Y. Barkov

Received: 15 February 2021
Accepted: 23 March 2021
Published: 26 March 2021

1. Introduction

The Eastern Tianshan orogenic belt is located in the southern margin of the Paleo-Asian Ocean. It is a convergence region between the Siberian Craton and the Tarim Craton, which has experienced a very complex process [1]. A series of magmatic Ni-Cu sulfide deposits occur in the Eastern Tianshan region, which is an important Ni-Cu resource base in China. All of these deposits are hosted in mafic-ultramafic intrusions. Most of the intrusions are located along the Jueluotage Belt, such as the Tudun, Huangshan, and Tulaergen mafic-ultramafic intrusions. A few of them are located in the Middle Tianshan Terrane, including the Tianyu and Baishiquan intrusions. It was demonstrated that the ages of these mafic-ultramafic intrusions range from 269 Ma to 300 Ma [2–10], indicating that most of the intrusions formed in the Early Permian. The parental magma of these mafic-ultramafic intrusions is tholeiitic, derived from a subducted slab-metasomatized mantle source, which has experienced different degrees of crustal contamination and sulfide segregation [11–17].

The formation of deposits is closely related to their specific tectonic settings [18]. However, the tectonic settings of the magmatic Ni-Cu ore-bearing mafic-ultramafic intrusions in the Eastern Tianshan orogenic belt remain controversial. Present viewpoints are as follows:

1. post-collision extension background [12,19–21]; 2. related to mantle plume [3,22–27]; 3.orgenic belt overlapped with mantle plume [18,28–31]; 4. products of subduction combined with mantle plume [32,33]; 5. Alaskan-type intrusions, originated from an island arc environment [5,34–36]. What causes the controversies above includes whether the Paleo-Asian Ocean had closed or not when the intrusions intruded, and whether the mantle plume made a contribution to the formation of the intrusions.

Nonetheless, there are also different opinions on the Paleo-Asian Ocean's final closure time. Different research teams hold different views, including Early to Middle Devonian [37], Late Devonian to Early Carboniferous [38–40], end of Devonian [33,41], Late Devonian to Carboniferous [42], Late Devonian to Early Permian [43], Late Carboniferous to Early Permian [44], Early Triassic [34]. Most researchers believe that the closure occurred during the Late Carboniferous [45].

The Baixintan Ni-Cu ore-bearing mafic-ultramafic intrusion was discovered in 2012 by the No. 1 Regional Geological Survey Party of Xinjiang Geology and Mineral Development Center [46]. To date, it is a medium-sized Ni-Cu deposit that contains 842.1 million metric tons (Mt) of sulfides ores with average grades of 0.59 wt. % Ni and 0.76 wt. % Cu. In this study, we established the age of the Baixintan intrusion by using the zircon SHRIMP (Sensitive High Resolution Ion MicroProbe) U-Pb dating. In addition, the geochemical characteristics, including the whole-rock geochemistry and the Sr-Nd isotopes, were analyzed. To discuss the magma source and tectonic setting of the Baixintan intrusion, a comparison was made between the Baixintan intrusion and intrusions generated from arc-related and mantle plume settings.

2. Regional Geology

The Central Asian Orogenic Belt (CAOB), sandwiched between the Siberian and Tarim Cratons, extends across Central Eurasia for almost 5000 km (Figure 1a). As an important part of CAOB, the Eastern Tianshan orogenic belt in Xinjiang Province is bounded by the Tu-Ha Basin to the north and the Beishan Rift to the south (Figure 1b), which can be divided into the Dananhu-Tousuquan island arc, the Jueluotage Belt, and the Middle Tianshan Terrane from north to south by the Kangguertage Fault and the Aqikuduke Fault. The Jueluotage Belt can be further divided into the Kangguer-Huangshan ductile-shear zone and the Yamansu back-arc basin by the Yamansu-Kushui Fault. A lot of Ni-Cu ore-bearing mafic-ultramafic intrusions have been discovered in the Jueluotage Belt, extending from east to west, such as Tulaergen, Huangshan, and Tudun [3,8,11]. On the south side of the Eastern Tianshan orogenic belt, the Baishiquan and Tianyu intrusions are located in the Middle Tianshan Terrane [7,47]. Several intrusions were produced in the Beishan Rift, such as Poyi, Luodong, Bijiashan, Hongshishan, and Xuanwoling [27,48–51] (Figure 1b).

The Baixintan intrusion occurs in the Dananhu-Tousuquan island arc, the southern margin of Tu-Ha Basin (Figure 1b). The formation of the Dananhu-Tousuquan island arc is closely related to the Paleozoic accretionary process of CAOB. The Devonian to Carboniferous sedimentary-volcanic rocks and intermediate-acid intrusive rocks are widely outcropped in the Dananhu-Tousuquan island arc [52–54]. The sedimentary-volcanic rocks consist of the Lower Devonian Dananhu Group and Tulaergen Group, Middle-upper Devonian Tousuquan Group, and Lower Carboniferous Qishan Group. The intrusive rocks mainly consist of granite, granodiorite, and monzonitic granite, and the magmatism in the arc lasts from the Silurian to the Carboniferous [55,56]. The subduction of the arc is thought to have ended by the Carboniferous [57,58]. The Kangguer-Huangshan ductile shear zone to the south of the Dananhu-Tousuquan island arc is a multiphase active and long-lasting ductile deformation metamorphic zone, characterized by strong compression and strike-slip. It is composed of a set of strata that have undergone strong deformation, including the Lower Carboniferous Gandun Group and the Wutongwozi Group volcanic sedimentary rocks [59]. A series of secondary faults derived from the main fault control the magmatism in the region [60].

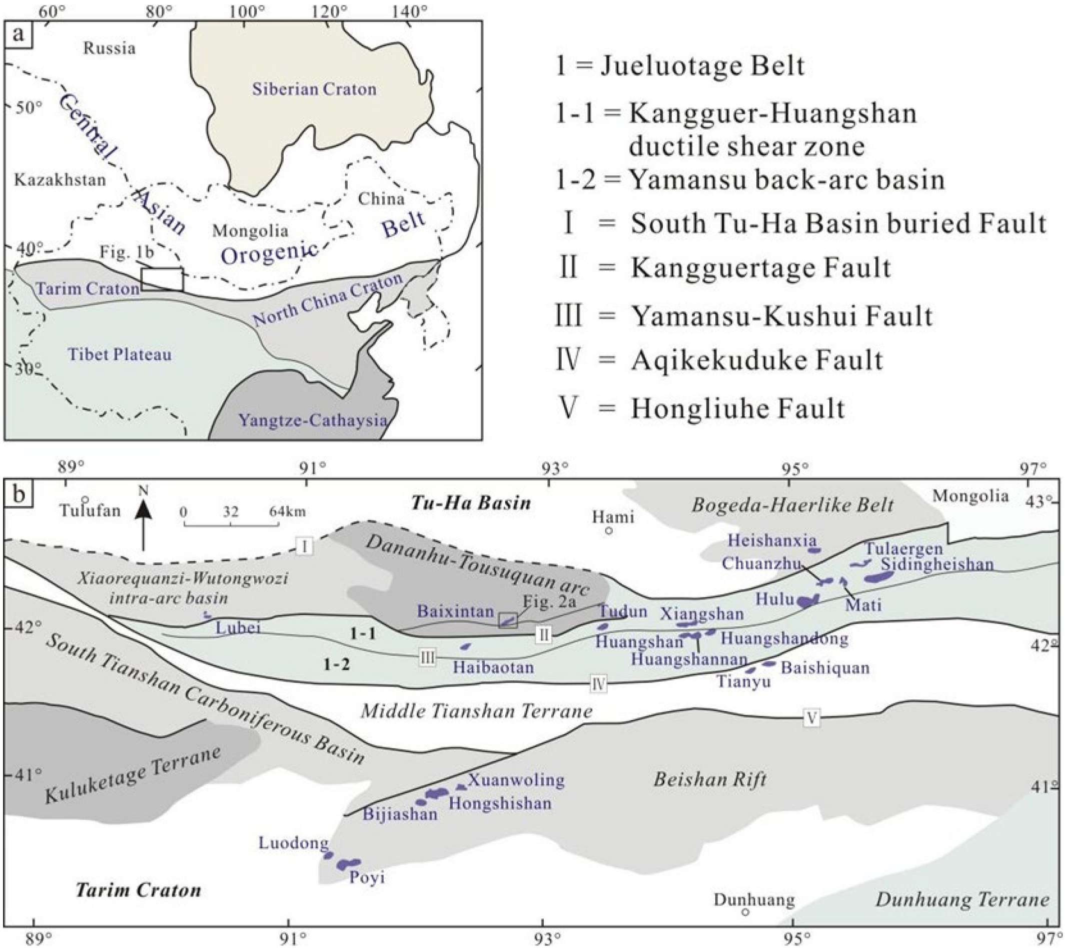

Figure 1. (**a**) Simplified geological map showing the location of the study area in the Central Asian Orogenic Belt (CAOB) (modified by [60]); (**b**) distribution of Ni-Cu ore-bearing mafic-ultramafic intrusions in the Eastern Tianshan orogenic belt and Beishan Rift (modified from [33,61–63]).

3. Petrography and Mineralization

To the north of the Dacaotan Fault, the Baixintan intrusion occurs in the Middle-Upper Ordovician Qiaganbulake Group, which consists of basalt, andesite, dacite, vocanic breccia, and tuff (Figure 2a). To the south of the Dacaotan Fault, the Lower Jurassic Badaowan group is exposed which consists of conglomerate, sandstone, and siltstone. The intrusion has a gourd shape, with an exposed area of 1.5 km^2, and a length of 2800 m. Monzonitic granite and granodiorite of Late Paleozoic age occur on the southern side of the Baixintan intrusion. The zircon U-Pb ages of granodiorites range from 358.14 Ma to 367.85 Ma [64]. The Baixintan intrusion is well-differentiated from north to south. It consists of lherzolite, olivine gabbro, and gabbro. The contacts between the gabbro, olivine gabbro and lherzolite are generally gradational. The ore bodies are lentoid, and are mainly hosted within lherzolite and gabbro (Figure 2b,c). Disseminated and patchy sulfides are the most important types of mineralization, massive and semi-massive sulfides are rare and only present in the basal contacts of the intrusion with country rocks [10].

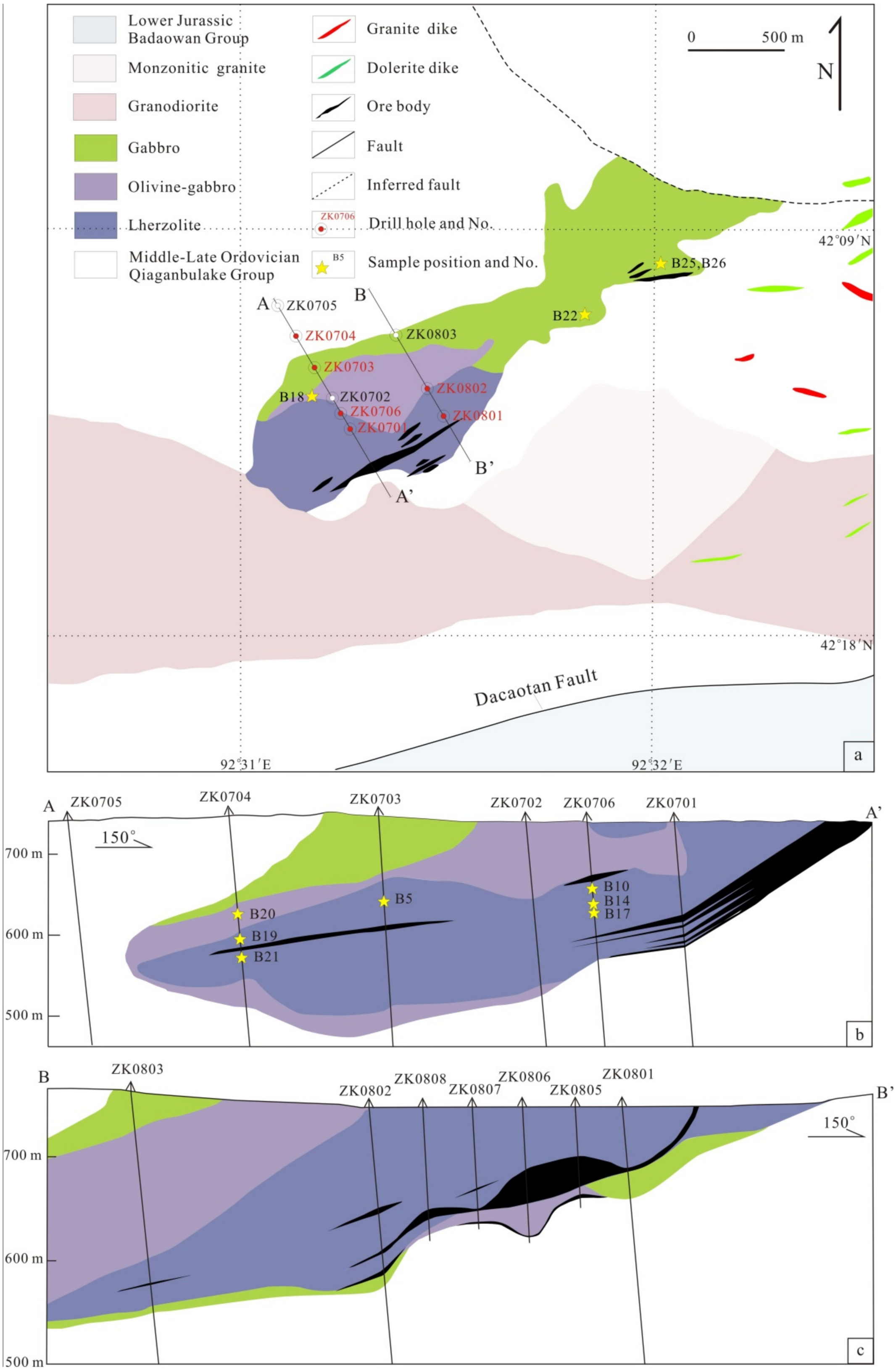

Figure 2. (**a**) The simplified geological map of the Baixintan intrusion; (**b**) cross section A-A′; (**c**) cross section B-B′ (modified from [65]). The near vertical lines in (**b**) and (**c**) are drill holes.

Lherzolite is located in the southwest of the intrusion. The lherzolite is composed of 60% olivine, 20% clinopyroxene, 15% orthopyroxene, and 3% plagioclase (Figure 3a,c). The olivines are surrounded by pyroxenes (Figure 3c). The ore minerals include pyrrhotite (Po), pentlandite (Pn), and chalcopyrite (Ccp) (Figure 3b).

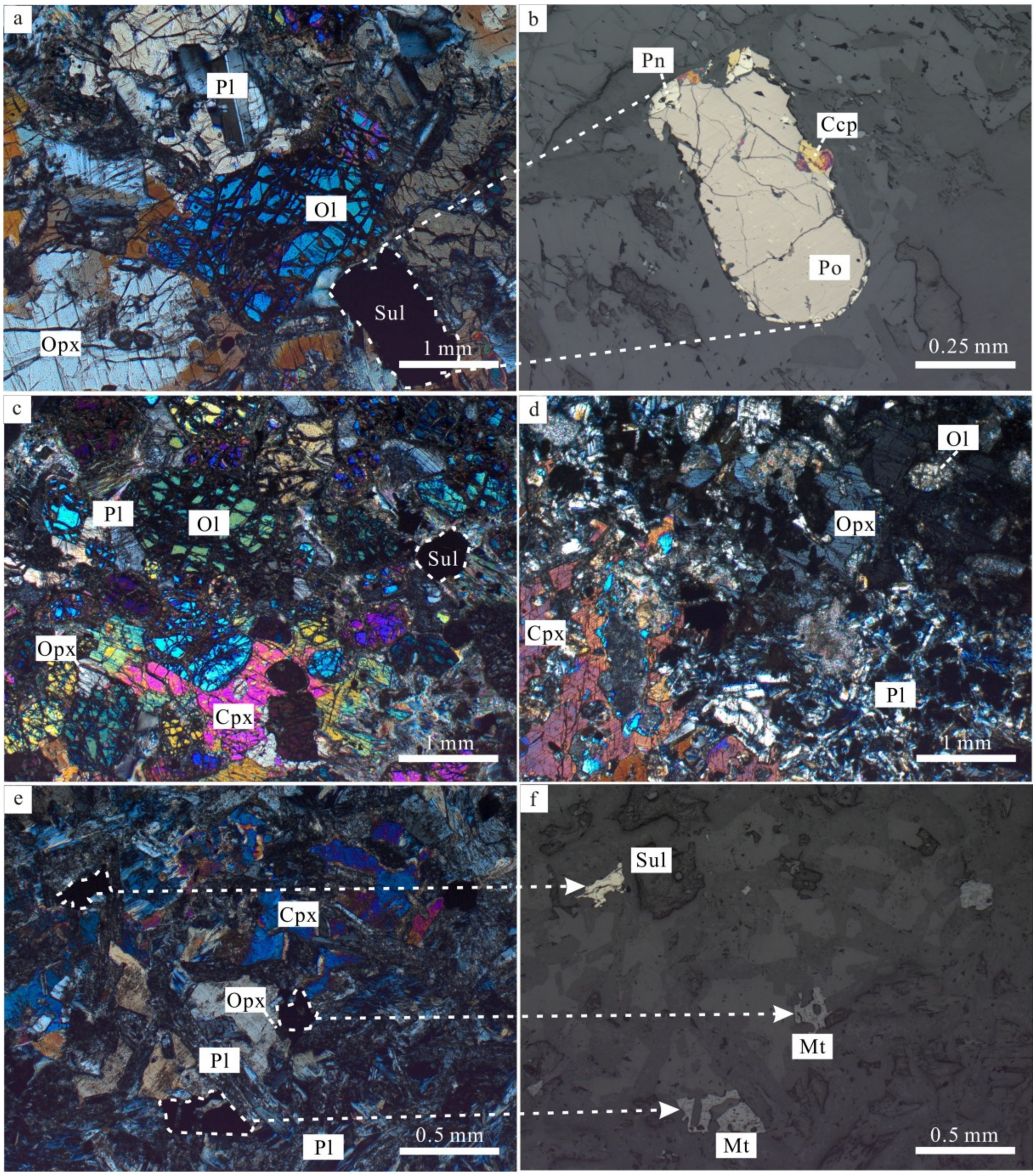

Figure 3. Microphotographs of rocks in the Baixintan intrusion. (**a**–**c**) Sulfide-bearing lherzolite; (**d**) olivine gabbro; (**e**,**f**) gabbro. Ol = olivine, Opx = orthopyroxene; Cpx = clinopyroxene; Pl = plagioclase, Sul = sulfide, Po = pyrrhotite, Pn = pentlandite, Ccp = chalcopyrite, Mt = magnetite.

Olivine gabbro is located in the center of the intrusion. It contains 25% clinopyroxene, 15% orthopyroxene, 35% plagioclase, and 30% olivine (Figure 3d).

Gabbro is the most widely distributed rock, which consists of 45% plagioclase, 40% clinopyroxene, and 10% orthopyroxene (Figure 3e). The rock contains sporadic sulfides and magnetite (Figure 3f).

4. Analytical Methods

4.1. SHRIMP Zircon Analyses

A fresh olivine gabbro sample (BXT-B18) from the Baixintan intrusion was selected for zircon U-Pb dating, and the sample location is shown in Figure 2a. Zircons were separated using conventional heavy liquid and magnetic techniques at the Langfang

Regional Geological Survey Lab in the Hebei Province. Zircons were hand-picked by using a binocular microscope and were selected by choosing the clearest, crack and inclusion-free grains. All zircon grains were inspected by backscattered scanning electron (BSE) microscope (Carl Zeiss AG, Jena, Germany) and cathodoluminescene (CL) microscopy (Gatan lnc, Las Vegas, NV, USA), to investigate their internal microstructures and check the position of the analytical spot with respect to the microstructures. U-Pb dating was carried out using the SHRIMP II ion microprobe at the Beijing SHRIMP Center, CAGS (Australian Scientific Instruments Pty Ltd, Canberra, Australia). The analytical procedure for zircon was similar to that described by [66,67]. The intensity of the primary $^{2-}$O ion beam was 4–6 nA. The primary beam size was ~30 μm, and each analytical site was rasterized for 2–3 min before analysis. Five scans through the relevant mass stations were made for each analysis. The standard zircon sample M257 (U = 840 ppm) was measured to calibrate U concentrations [68], and the standard zircon TEMORA (416.8Ma) was used for the isotopic fractionation correction [69]. A correction for common lead was made by measuring the ^{204}Pb amount. The common lead composition was calculated at ^{207}Pb/^{206}Pb measured ages, using the Stacey and Kramers model [70]. The data processing was carried out using the SQUID 1.03d and ISOPLOT 3.75 programs [71,72]. Uncertainties for individual analyses are quoted at the 1σ level, whereas errors for weighted mean ages are quoted at 95% confidence.

4.2. Whole-Rock Major and Trace Elements Analyses

The major elements and trace elements in whole rocks were analyzed at the Key Laboratory for the Study of Focused Magmatism and Giant Ore Deposit, MNR in Xi'an, China. Major elements were analyzed by using an Axio-type XRF instrument. After one hour of heating at 1000 °C, the loss-on-ignition (LOI) was determined by the weight loss of a powdered sample. The sample powders (0.7 g), were fused with 5.200 ± 0.001 g of lithium tetraborate ($Li_2B_4O_7$), 0.400 g ± 0.001 g lithium fluoride (LiF) and 0.30 ± 0.01 g ammonium nitrate (NH_4NO_3). The mixtures were dissolved in 1 mL lithium bromide solution at 1150–1250 °C for 10–15 min. The precision of the major elements was better than 2%. The accuracy and reproducibility were monitored by the Chinese national standard GBW07104 (andesite), and the standard values for GBW07104 are given in [73]. The standard deviation of the standard is better than 1%.

The trace elements were determined by using an ELEMENT inductively coupled plasma mass spectrometer (ICP-MS) by Thermo Fisher. Fifty-milligram powders of samples were dissolved in 1 mL of HF that was mixed with 0.5 mL of HNO_3 in a screw-cap capsule at 185 ± 5 °C for 24 h. The sample solutions were dissolved again in 0.5 mL HNO_3 in the capsules. After the solutions were dried, the previous step was repeated. The solutions were dissolved in 5 mL HNO_3 again in a capsule at 130 °C for 3 h. Finally, the solutions were diluted with H_2O to 50 mL for trace element analysis. The Chinese national standard GBW07105 (basalt) was used to monitor accuracy and reproducibility, and the standard values for GBW07105 are from [73]. The standard deviation of the standard is better than 3%. The precision is better than 5%.

4.3. Whole-Rock Sr-Nd Isotopes Analyses

Strontium and Nd in whole-rock samples were separated by using standard ion-exchange techniques [74]. Strontium and Nd isotopic analyses were performed on a Thermo Fisher Scientific Multi-receiving inductively coupled plasma mass spectrometer (MC-ICP-MS) at the National Research Center for Geoanalysis in Beijing, China (Thermo Fisher Scientific lnc, Waltham, MA, USA). The main analysis process is as follows: 0.25 g whole-rock powders were digested in sealed Teflon bombs with a mixture of 0.5 mL HNO_3 and 1.5 mL HF. The sealed bombs were kept in an oven at 190 °C for 48 h. The decomposed samples were then dried at 160 °C, followed by adding 3 mL 1:1 HNO_3. The solution was sealed and dissolved again at 150 °C for 6 h. An appropriate amount of aliquot was centrifuged, and the obtained supernatant was dried, followed by adjusting the pH. The solution containing Sr and Nd was separated by using SR specific resin and LN specific resin, respectively. The $^{87}Sr/^{86}Sr$ and $^{143}Nd/^{144}Nd$ ratios were determined on the Neptune Plus MC-ICP-MS. The measured $^{87}Sr/^{86}Sr$ and $^{143}Nd/^{144}Nd$ ratios were normalized to $^{88}Sr/^{86}Sr$ = 8.375209 and $^{1436}Nd/^{144}Nd$ = 0.7219, respectively. The uncertainty of $^{87}Sr/^{86}Sr$ and $^{143}Nd/^{144}Nd$ values is given as 2σ.

4.4. Whole-Rock Ni, Cu, S and Platinum-Group Elements Analyses

Whole-rock Ni and Cu contents were determined using the Varian ICP735-ES inductively coupled plasma emission spectrometer and the Perkin Elmer Elan 9000 inductively coupled plasma mass spectrometer (ICP-MS) at the ALS Chemex (Guangzhou, China) Co. Ltd., respectively. The analytical precisions are ~7% and ~4% for Ni and Cu, respectively. Whole-rock S contents were measured by using a gravimetric method and IR absorption with the detection limits ~0.01%. The analytical precisions are ~4% of amount present for S. The values of standards GXR-1 and GXR-3 are from [75] and given in Table A5.

The concentrations of platinum-group elements (PGE) were determined by nickel sulfide fire assay-inductively coupled plasma mass spectrometry at the National Research Center of Geoanalysis in Beijing, China (PerkinElmer, Waltham, MA, USA). The precision and accuracy were monitored via analyses of the standards GBW07290 and GBW07291, and the recommended values and analytical values are from [73]. The analytical procedure was similar to that described by [76,77].

5. Analytical Results

5.1. SHRIMP Analyses

The zircons separated from olivine gabbro are subhedral with a length of 60–140 μm and an elongation (length-to-width) ratios of 1–1.5, respectively. The grains are mostly homogeneous un-zoned and well defined with sharp tips (Figure 4a), and are similar with the igneous zircons described by [78]. The Th contents of the selected grains range from 544 ppm to 2709 ppm, and those of U range from 294 ppm to 1455 ppm. The relatively high Th/U ratios (0.95–2.38) of the zircons indicate their magmatic origin [79]. Among the zircon grains from sample BXT-B18 (Figure 4a), twenty-one grains (No. 1—No. 21) give concordant data within the error (Figure 4b), with $^{206}Pb/^{238}U$ age ranging from 272.4 ± 1.9 to 280.3 ± 2.3 Ma. (Table A1). The 21 analyses yield a mean $^{206}Pb/^{238}U$ age of 276.8 ± 1.1 Ma (95% confidence level, 2σ, MSWD = 1.8, probability = 0.020, see Supplementary Materials, Table S1. SHRIMP zircon U-Pb age data of sample BXT-B18 from the Baixintan intrusion) (Figure 4b).

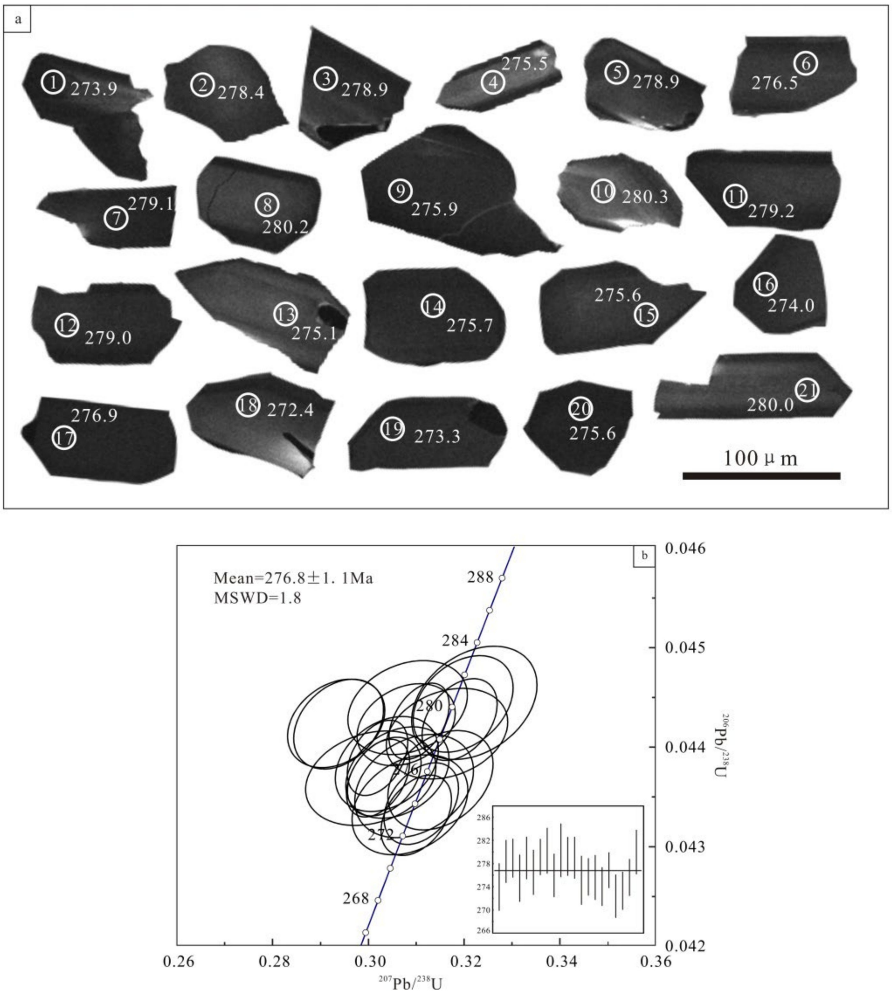

Figure 4. (**a**) Cathodoluminescence images of selected zircon crystals from Baixintan olivine gabbro (BXT-B18); (**b**) Zircon U-Pb isotope concordia plot. Circles are analytical positions, and numbers are $^{206}Pb/^{238}U$ ages (in the unit of Ma).

5.2. Major Oxides and Trace Elements

The whole-rock major and trace element results are listed in Table A3. Ten samples from the Baixintan intrusion including lherzolite, olivine gabbro, and gabbro were selected for analysis. The compositional ranges of these samples are as follows: SiO_2 = 40.75%–48.42%, Al_2O_3 = 5.02%–18.04%, MgO = 7.93%–32.28%, TFeO = 5.49%–11.86%, CaO = 2.62%–10.09%, Na_2O+K_2O = 0.88%–3.91%, $Mg^{\#}$ = 62.26–83.11.

Compared to the primitive mantle and chondrite, the samples from the Baixintan intrusion are enriched in large ion lithophile elements (LILE), such as K, Sr, and Ba, and show strongly negative Nb, weakly negative Ta and Ti anomalies (Figure 5a). Except for one sample, Sr is enriched strongly, and U is enriched in some samples (Figure 5a).

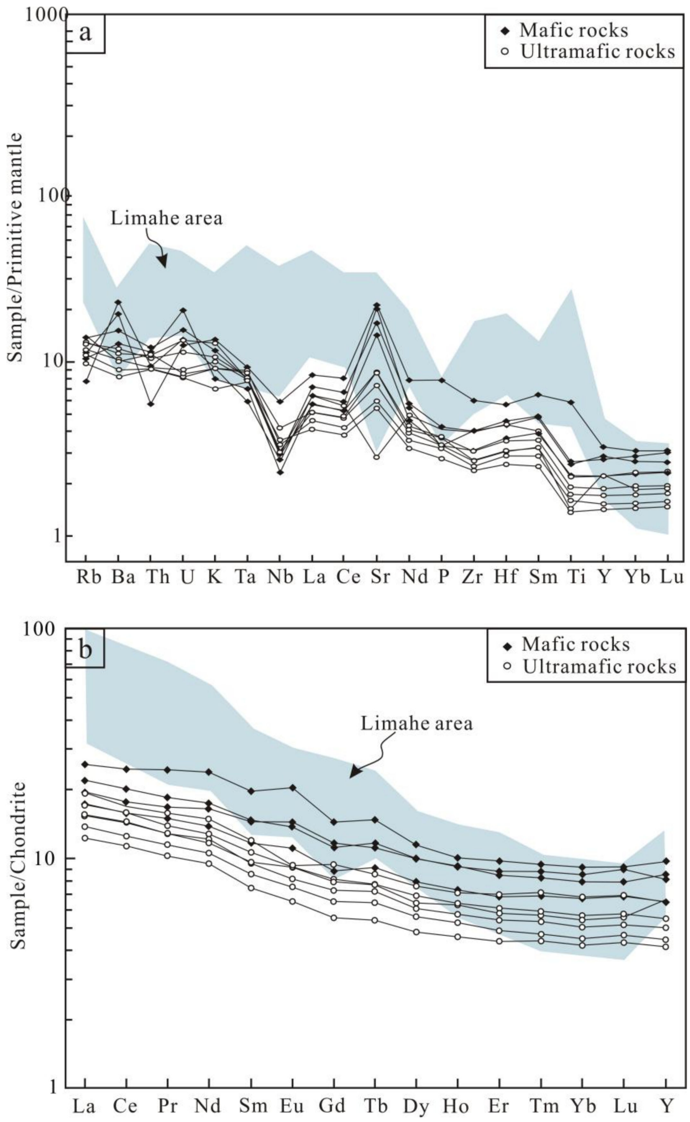

Figure 5. (**a**) Primitive mantle normalized incompatible trace element spider diagram; (**b**) Chondrite-normalized REE patterns for samples from the Baixintan and Limahe intrusions. Data sources of Limahe (25 samples): [80,81]. The primitive mantle values and chondrite values are from [82].

The ΣREE, LREE, and HREE values of the samples are 27.78–64.52, 16.79–38.68, and 10.98–25.84 ppm, respectively. They are enriched in LREE relative to HREE, with a LREE/HREE ratio of 1.24–1.58, exhibiting right-leaning patterns (Figure 5b). There are weak positive Eu anomalies in most mafic rocks, which are absent in ultramafic rocks (δEu = 0.87–1.20).

5.3. Sr and Nd Isotopes

The Rb-Sr and Sm-Nd isotopic data are listed in Table A4. The $^{87}Sr/^{86}Sr$ ratios of samples are between 0.036 and 0.548. The initial $^{87}Sr/^{86}Sr$ ratios are relatively low, with a range from 0.7035 to 0.7044. The $^{147}Sm/^{144}Nd$ and the initial $^{143}Nd/^{144}Nd$ are 0.1504–0.1799 and 0.5125–0.5127, respectively. All the samples have positive calculated εNd (t) values, ranging from +4.50 to +7.70, with an average of +5.31. The relatively low initial $^{87}Sr/^{86}Sr$ ratios and positive εNd (t) values of the Baixintan intrusion are similar to typical Ocean Island Basalt (OIB) (Figure 6).

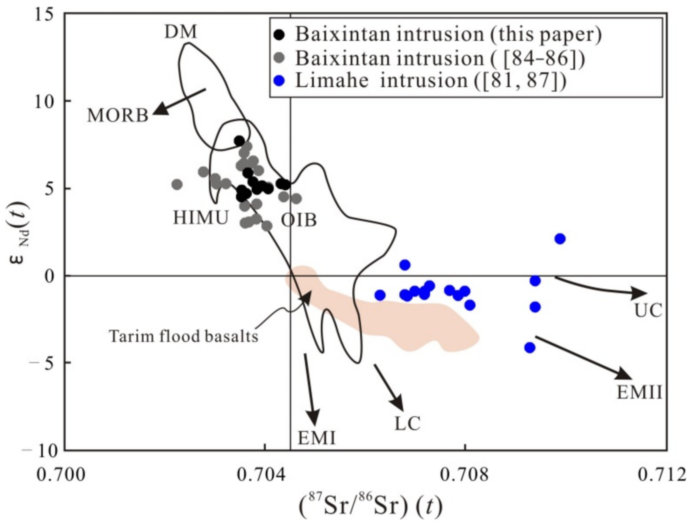

Figure 6. $^{87}Sr/^{86}Sr(t)$-εNd(t) diagram (after [83]). Data sources of Baixintan: this paper, [84–86]; data sources of Limahe: [81,87];data sources of Tarim flood basalts: [88–90].

5.4. Ni, Cu, S and PGE Concentration

The analytical results for Ni, Cu, S, and PGE are listed in Table A5. The PGE contents of rocks from the Baixintan intrusion are relatively low: the contents of ΣPGE range from 0.65 ppb to 4.85 ppb, with an average of 2.50 ppb, which is obviously depleted relative to the primitive mantle (ΣPGE = 23.5 ppb). The ΣPGEs of mafic rocks (gabbros) range from 0.65 ppb to 0.81 ppb, with an average of 0.71 ppb; the ΣPGEs of ultramafic rocks (lherzolites) range from 1.67 ppb to 4.85 ppb, with an average of 3.40 ppb. The mantle-normalized PGE patterns for the rocks from the Baixintan intrusion have an overall trough shape (Figure 7), showing that the rocks are depleted in PGEs relative to Ni and Cu, which are also characterized by depletions in Os, Ir, and Ru relative to Rh, Pt, and Pd. The Ni/Cu and Pd/Ir ratios of the Baixintan intrusions are 1.91–15.01 and 6.56–11.17, respectively. The Cu/Pd ratios range from 0.63×10^5 to 4.37×10^5.

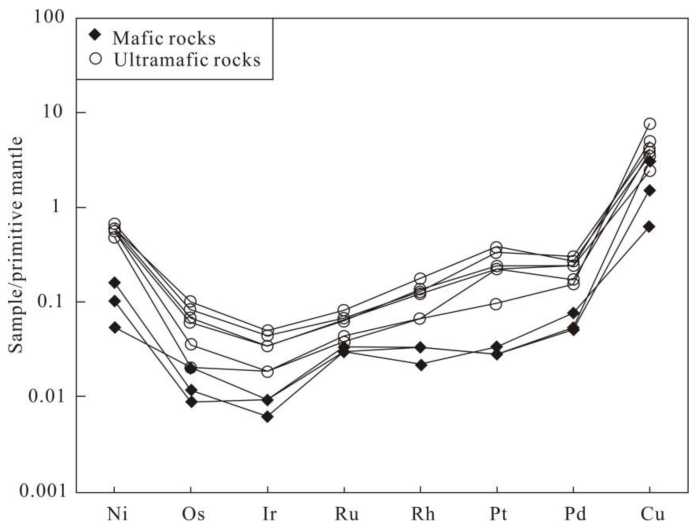

Figure 7. Primitive mantle-normalized platinum-group elements (PGE) patterns for the rocks from the Baixintan intrusion. The primitive mantle values are from [91].

6. Discussion

6.1. Parental Magma and Sulfide Segregation

As shown in Figure 8, the MgO and FeO contents show negative relationships with the SiO_2 content (Figure 8a,b), which is in agreement with the fractionation of olivine and chromite; the CaO and Al_2O_3 contents show positive relationships with the SiO_2 content (Figure 8c,d), which is consistent with the fractionation of clinopyroxene and plagioclase. The TiO_2 and the total alkali (K_2O + Na_2O) contents are positively related to the SiO_2 content (Figure 8e,f). In the alkaline-silica diagram, all the samples plot in the subalkaline field (Figure 8f). In the AFM (Na_2O + K_2O-FeO-MgO) diagram, the ultramafic rocks show a tholeiitic trend, and the mafic rocks are closer to the calc-alkaline trend (Figure 9).

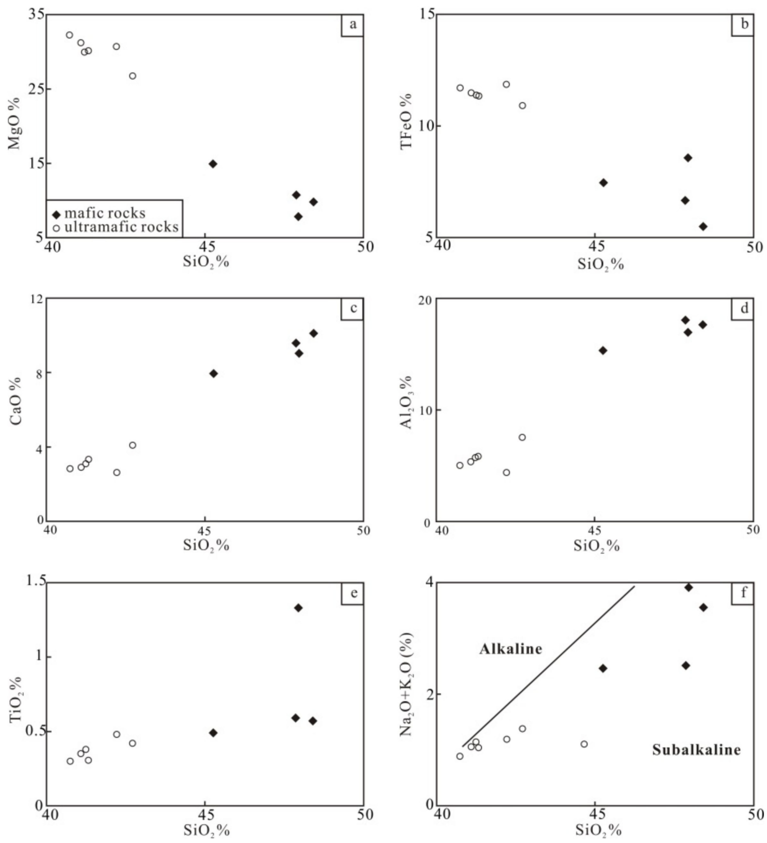

Figure 8. Harker diagrams (**a**–**e**) and alkaline-silica diagram (**f**) for the mafic-ultramafic rocks of the Baixintan intrusion (after [92]).

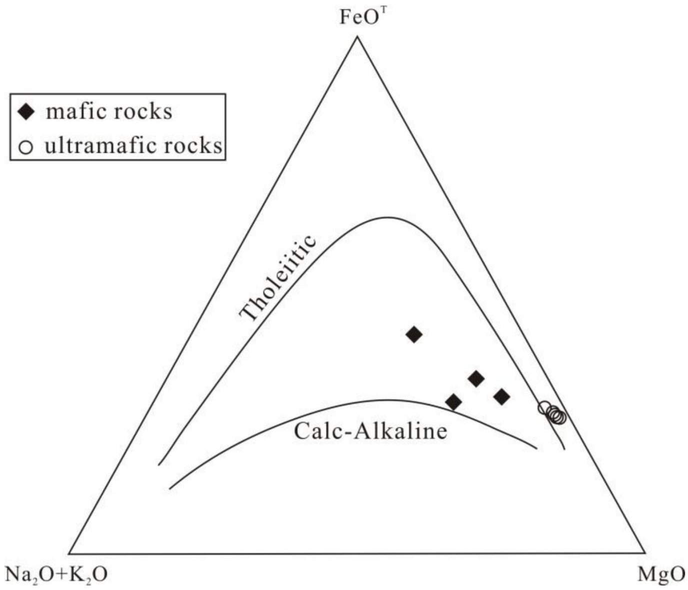

Figure 9. AFM diagram for the mafic-ultramafic rocks of the Baixintan intrusion (after [92]).

In a plot of Ni/Cu (1.91–15.01) and Pd/Ir (6.56–11.17) ratios, the majority of the mafic-ultramafic rocks from the Baixintan intrusion fall into the area of layered intrusions, close to the high-Mg basalts region (Figure 10), indicating that the parental magmas for the Baixintan intrusion were likely high-Mg basalt in composition. The rocks from the Baixintan intrusion have relatively consistent Pd/Ir ratios but variable Ni/Cu ratios. On average, the ultramafic rocks seem to have higher Ni/Cu ratios than the mafic rocks, and are consistent with the "olivine removal" trend (Figure 10). Moreover, Feng et al. [10] found that the parental magma for the Baixintan intrusion was depleted in PGE, and the Ir and Pd contents in the parental magma were estimated at ~0.0022 ppb and ~0.18 ppb, respectively.

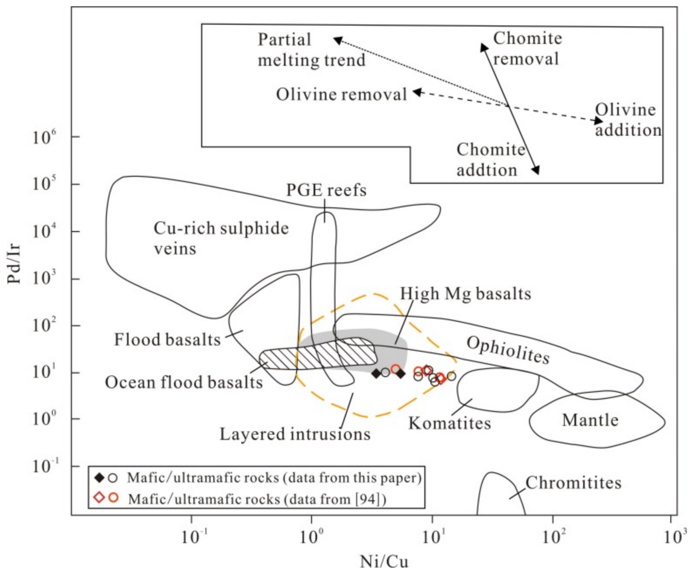

Figure 10. Ni/Cu-Pd/Ir diagram of the rocks from the Baixintan intrusion (after [93]). Data are from this paper and [94].

The host magma becoming saturated in sulfide and segregating immiscible sulfide is one of the key aspects in the genesis of a magmatic sulfide ore deposit [95]. Because the elemental compatibilities of PGEs in rock-forming minerals are quite different, we can use the correlations of the PGEs and the Cu/Pd ratios to reveal the sulfide segregation process of the parental magma [96].

The estimated bulk solid-liquid partition coefficients for PGE, Ni, and Cu in a very differentiated komatiitic basalt are Ir 6.6, Ru 4.5, Pt 0.53, Pd 0.09, Ni 6.2, Cu, 0.01 [97]. Iridium is compatible in clinopyroxene, but incompatible in olivine; Rh is compatible in olivine, but incompatible in both clinopyroxene and orthopyroxene; Pt is compatible in orthopyroxene, but incompatible in olivine and clinopyroxene; Pd and Cu are incompatible elements in all of the minerals mentioned above [98–100]. Hence, if no sulfide saturation occurs, the PGEs will become progressively fractionated [93], the fractional crystallization of the mafic minerals can give rise to the decrease of the Ni, Ir, and Rh contents, but increases the Pt, Pd, and Cu contents in the residual magma. Consequently, the Pd/Ir ratios of the residual magma increase significantly, while the Cu/Pd ratios remain stable [96]. Once sulfide saturation occurs, most of the PGEs will tend to enter the sulfide [93], which causes a strong loss of PGEs in the parental magma, while the contents of Ni and Cu decrease slightly. Consequently, the Pd/Ir ratios in the residual magma remain stable, while the Cu/Pd ratios increase significantly [96].

With the decrease of Ir, the contents of Rh, Pt, and Pd in the rocks from the Baixintan intrusion decrease rapidly (Figure 11a–c). A positive correlation between Pt and Pd can be seen in the rocks (Figure 11d). The Cu/Pd ratios of rocks from the Baixintan intrusion range from 0.63×10^5 to 4.37×10^5 (Table A5), which are distinctly higher than that of the primitive mantle (10^3–10^4, [95]). The Pd/Ir ratios of the samples do not vary a lot (Figure 10), ranging from 6.56 to 11.17 (Table A5). The positive correlations between PGEs and the higher Cu/Pd ratios of samples from the Baixintan intrusion indicate that the parental magma has experienced a sulfide segregation process. Ruan et al. [101] considered that the assimilation of crustal Si and S components played important roles on sulfide segregation in the parental magma of the Baixintan intrusion.

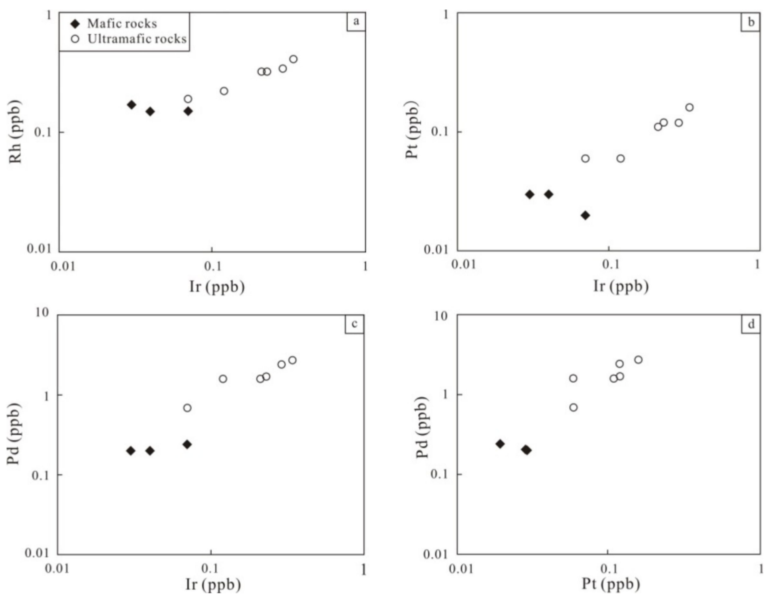

Figure 11. (**a**) Rh-Ir diagram; (**b**) Pt-Ir diagram; (**c**) Pd-Ir diagram; (**d**) Pd-Pt diagram for rocks from the Baixintan intrusion.

6.2. Tectonic Settings and Magma Source

In this part, this paper will estimate the tectonic setting and the magma source of the Baixintan intrusion by comparing it with other two specific mafic-ultramafic intrusions, such as the Limahe and Duke Island intrusions, which are generated in different acknowledged tectonic settings. The Limahe intrusion is located in the Emeishan Large Igneous Province (ELIP), SW China. The ELIP is composed of huge volumes of Emeishan flood basalts, numerous mafic-ultramafic intrusions, granites, and syenites [102]. The genetic relationship between the mafic-ultramafic intrusions emplaced in the ELIP and the mantle plume has been discussed in previous studies [87,103–111]. The Duke Island intrusion, located in Southeastern Alaska, is generally regarded as a zoned Alaskan-type intrusion [112–115].

6.2.1. Is Baixintan an Alaskan-Type Intrusion?

Some researchers held the view that the Ni-Cu ore-bearing mafic-ultramafic intrusions (or some of them) located in the Eastern Tianshan orogenic belt are Alaskan-type intrusions which are formed in the island arc or active continental margin because of their zoned bodies and some arc-like geochemical characteristics, such as relatively high large ion lithophile elements (LILE) and low high field strength elements (HFSE), negative anomalies of Nb and Ta [5,34–36]. Most of the classic Alaskan-type intrusions show the following characteristic features [113]: 1. rock types that are mostly dunite, wehrlite, olivine clinopyroxenite, magnetite-rich clinopyroxenite, and gabbro; 2. crude concentric zoning in some of the larger bodies with dunite in the central-most parts and gabbro in the outer-most parts; 3. principal mineral associations in the ultramafic rocks consisting of olivine, diopside, magnetite, and hornblende, orthopyroxene and plagioclase are characteristically absent. The mineral assemblage of Alaskan-type intrusions means that the rocks ought to be depleted in SiO_2 and enriched in CaO, especially for the pyroxenites [116]. In the CaO-SiO_2 discrimination diagram (Figure 12), samples from the Duke Island intrusion are invariably plotted into the Alaskan field. However, all the samples from the Baixintan intrusion, as well as the Limahe intrusion are plotted into the layered intrusion field, showing lower CaO contents. As we can see in Figure 13, the spinel compositions of the Baixintan and Limahe intrusions are quite different from that of Alaskan-type zoned ultramafic intrusions. Samples from the Limahe intrusion falls into the area of "Subvolcanic intrusions related to flood basalts", samples from the Baixintan intrusion are plotted into the "Layered intrusions", and most of them are precisely distributed along the right margin of "subvolcanic intrusions related to flood basalts".

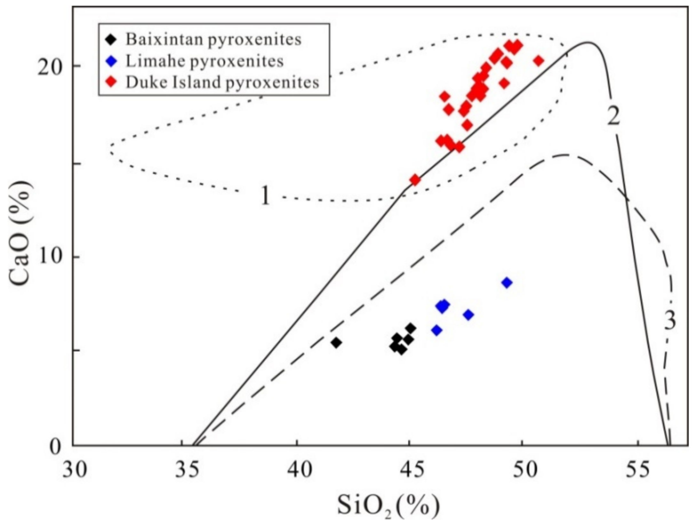

Figure 12. SiO_2-CaO diagram of pyroxenites from the Baixintan, Limahe, and Duke Island intrusions (after [116]. 1 = Alaskan field, 2 = Ophiolitic field, and 3 = Layered intrusion field. Data source of Baixintan: [84]; data sources of Duke Island: [114,115]; data sources of Limahe: [80].

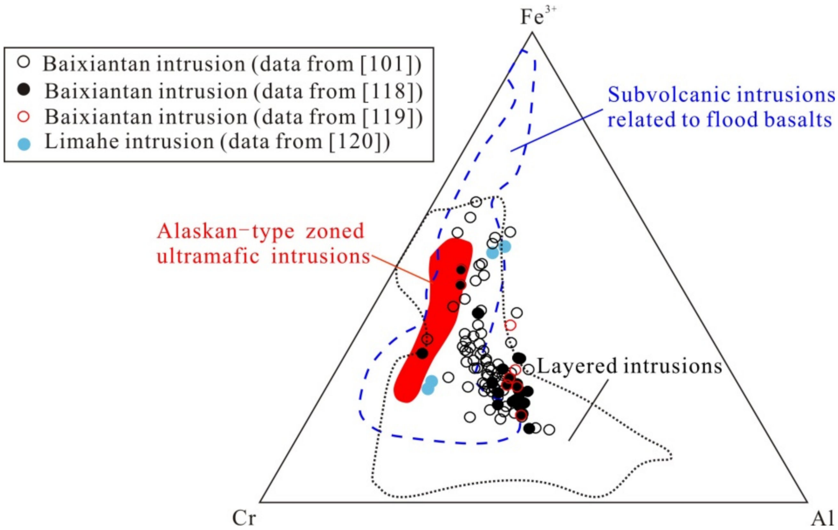

Figure 13. Trivalent ion plots for the Baixintan and Limahe intrusions [117]. Data sources of Baixintan: [101,118,119]; data source of Limahe: [120].

Based on the evidences from the compositions of pyroxenite and spinel, we consider that the Baixintan intrusion is not an Alaskan-type intrusion.

6.2.2. What Caused the Negative Anomalies of Nb, Ta, and Ti in the Baixintan Intrusion?

It was demonstrated that contamination by continental crust or lithosphere, or a metasomatized source by the subduction-related fluids can give rise to negative Nb, Ta, and Ti anomalies [121]. By contrast, uncontaminated plume-generated basaltic rocks will normally have flat REE patterns or LREE-enriched patterns and lack negative Nb, Ta, and Ti anomalies [122–124]. Compared with the plume-derived Limahe intrusion, samples from the Baixintan intrusion have strongly negative Nb, weakly negative Ta and Ti anomalies (Figure 5a) and relatively flat REE patterns (Figure 5b). Feng et al. [10] stated that the Baixintan mafic-ultramafic intrusive rocks are characterized by moderate light REE enrichments relative to heavy REE and pronounced negative Nb-Ta anomalies. The prominent negative Nb-Ta anomalies in the Baixintan intrusion were also found by the authors of [84,125]. However, most samples from the Baixintan intrusion are plotted into the ocean island basalt (OIB) area in the $^{87}Sr/^{86}Sr(t)$-εNd(t) diagram (Figure 6), implying that they are derived from a more enriched mantle source compared to MORB, which may be explained by mantle plume material. The lower $^{87}Sr/^{86}Sr(t)$ ratios and higher εNd(t) values compared with the Limahe intrusion also suggest the magma of the Baixintan intrusion may have experienced a lower degree of crustal contamination (Figure 6). In consideration of a low degree of crustal contamination suggested by the Sr and Nd isotopes, this paper tends to attribute the negative Nb, Ta, and Ti anomalies of the Baixintan intrusion to its metasomatized mantle source by subduction-related fluids.

This is also supported in the Ba/La-Th/Yb diagram (Figure 14). Rocks produced in oceanic subduction systems can be divided into two trends [126]. The high Ba/La trend is thought to be related to slab-derived fluids, and the high Th/Yb trend is attributed to either melting of subducted sediment or bulk assimilation of sedimentary material, intercalated within the volcanic pile, during magma ascent through the arc crust [126]. In the Ba/La-Th/Yb diagram (Figure 14), the Limahe intrusion displays a high Th/Yb ratio trend, while the Baixintan, similar to the Duke Island intrusion, follows a high Ba/La ratio trend. These features further indicate that: 1. the assimilation and contamination of crustal materials played a key role during the formation of the Limahe intrusion, which is consistent with the information reflected by the Sr and Nd isotopic characteristics (Figure 13); 2. the Baixintan intrusion may derive from a mantle source that is metasomatized by slab-derived fluids' components.

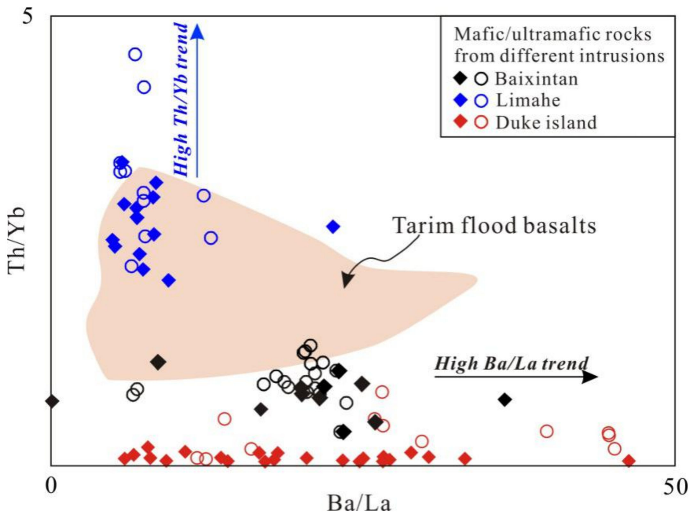

Figure 14. Ba/La-Th/Yb diagram (after [126]). Data sources of Baixintan: this paper, [84]; data sources of Limahe: [80,81]; data source of Duke Island: [115]; data sources of the Tarim flood basalts field (51 samples): [88,90,127,128].

Furthermore, previous studies have shown that subduction slab-derived fluids have made a contribution to the source of intrusions located in the Eastern Tianshan orogenic belt [11–17], but the contribution of subduction slab-derived fluids to the source of the Pobei and Hongshishan intrusions in the Beishan Rift was excluded [27,49,50,129,130]. It means that the scope of impacts on the intrusions by the subduction event is limited in the region. The impact of subduction seems to be weakened gradually from the Eastern Tianshan orogenic belt to the Beishan Rift.

6.2.3. A Proposed Plume-Related Back-arc Spreading Tectonic Setting for the Baixintan Intrusion

The Nb_N-Th_N discrimination diagram [131] displays possible tectonic settings for the Baixintan and the other two different types of mafic-ultramafic intrusions discussed previously (Figure 15a,b). In Figure 15a, most of the samples plot into the low-Ti island arc tholeiite (IAT) field, showing similar geochemical features with island arc tholeiites. Based on the discussion before, we consider that these arc-like features are caused by its metasomatized mantle source. In Figure 15b, nearly all of the samples from the Baixintan intrusion are limited to the Back-arc A field, implying a back-arc setting of Baixintan and an input of subduction components. In contrast, a large proportion of samples from the Limahe intrusion fall into the alkaline OIB and the overlap between OIB and P-MORB field (Figure 15a), which is consistent with its plume source. Moreover, there seems to be a trend of increasing the OIB-type component from the Baixintan to the Limahe intrusion (Figure 15b). Samples from the Duke Island intrusion fall into supra-subduction zone (Figure 15a), which is indicative of a nascent forearc convergent setting (Figure 15b).

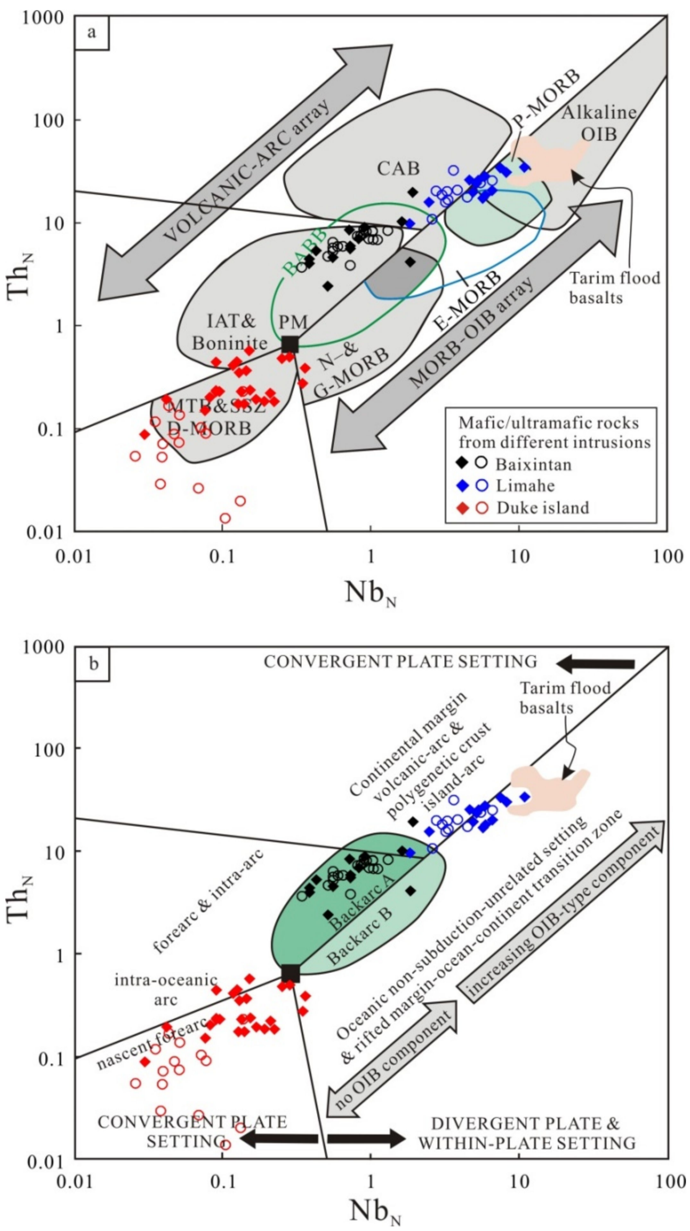

Figure 15. (**a**) The compositional variations of different intrusions on the Th$_N$-Nb$_N$ diagram; (**b**) tectonic interpretation of different intrusions based on Th$_N$-Nb$_N$ systematics (after [131]). Data sources are the same as in Figure 14. Abbreviations: MORB = mid-ocean ridge basalt, N-MORB = normal-type MORB, G-MORB = garnet-influenced MORB, E-MORB = enriched-type MORB, P-MORB = plume-type MORB, AB = alkaline ocean-island basalt, IAT = low-Ti island arc tholeiite, Boninite = very low-Ti boninitic basalt, CAB = calc-alkaline basalt, MTB = medium-Ti basalt, SSZ = supra-subduction zone, D-MORB = depleted-type MORB, BABB = back-arc basin basalt, Back-arc A = BABB characterized by input of subduction or crustal components, and Back-arc B = BABB showing no input of subduction or crustal components. In both panels, Nb and Th are normalized to the N-MORB composition [82].

The Early Permian Tarim large igneous province (TLIP) in North West China consists of two magmatic phases [132]: the ~290 Ma magmatic phase is characterized by bimodal volcanic rocks that consist of rhyolites and basalts, which occur within the Tarim Craton; the ~280 Ma magmatic phase is mainly composed of intrusive rocks and mafic dikes, which mainly appear on the northern border of the Tarim Craton and inside of the CAOB [25]. Recently, several zircon U-Pb ages of the Baixintan intrusion have been published. Zircon U-Pb LA-ICP-MS age of plagioclase-bearing lherzolite in the Baixintan intrusion is 277.9 ± 2.6 Ma [125], zircon U-Pb LA-ICP-MS age of olivine gabbro is 287.3 ± 3.1 Ma [84], and a U-Pb age of olivine norite (olivine gabbro in this paper) is 286.0 ± 1.6 Ma [10]. In this study, zircons separated from olivine gabbro yielded a SHRIMP U-Pb age of 276.8 Ma (Figure 4b), which is consistent with [125], but ~10Ma younger than the age reported by the authors of [10,84]. Even so, the ages obtained indicate that the Baixintan intrusion located in the Eastern Tianshan belt formed in the Early Permian, which is consistent with the later magmatic phase of the TLIP. Other ore-bearing intrusions in the Eastern Tianshan belt and the Beishan Rift formed almost simultaneously (Figure 1b, Table 1). Furthermore, the mafic-ultramafic intrusions are normally associated with A-type granites spatially and temporally, suggesting that these magmatic events occurred during an extensional regime, possibly related to a mantle plume event [25].

Table 1. Zircon U-Pb ages of intrusion located in the Eastern Tianshan orogenic belt and Beishan Rift.

Tectonic Units	Intrusions	Rock Types	Testing Methods	Ages (Ma)	Data Sources
Dananhu-Tousuquan arc	Baixintan	Olivine gabbro	SHRIMP	276.8 ± 1.1	This study
		Olivine norite	LA-MC-ICP-MS	286.0 ± 1.6	[10]
Xiaorequanzi-Wutongwuzi intra-arc basin	Lubei	Hornblende gabbro	LA-MC-ICP-MS	287.9 ± 1.6	[133]
Juluotage Belt	Huangshan	Diorite	SHRIMP	269 ± 2	[3]
	Huangshandong	Olivine norite	SHRIMP	274 ± 3	[2]
	Huangshannan	Gabbronorite	SIMS	282.5 ± 1.4	[134]
	Xiangshan	Norite gabbro	SHRIMP	285 ± 1.2	[1]
	Tudun	Hornblende gabbro	LA-ICP-MS	298.37 ± 0.94	[9]
	Hulu	Gabbro diorite	LA-ICP-MS	274.5 ± 3.9	[135]
	Tulaergen	Gabbro	SHRIMP	300.5 ± 3.2	[8]
Middle Tianshan Terrane	Tianyu	Gabbro	LA-ICP-MS	290 ± 3.4	[7]
	Baishiquan	Gabbro	SHRIMP	281 ± 0.9	[5]
Beishan Rift	Xuanwoling	Gabbro	SIMS	260.7 ± 2.0	[136]
	Hongshishan	Olivine gabbro	LA-ICP-MS	281.8 ± 2.6	[137]
	Bijiashan	Gabbro	SIMS	279.2 ± 2.3	[28]
	Luodong	Gabbro	SIMS	283.8 ± 1.1	[138]
	Poyi	Gabbro	SHRIMP	278 ± 2	[139]

In the Nb/Yb-Th/Yb discrimination diagram (Figure 16a), the oceanic basalts (intra-plate islands, plume-distal ocean ridges and oceanic plateau) plot predominantly within the MORB-OIB array (shaded), while crustally contaminated basalts and alkalic basalts containing a large recycled component mainly plot above the MORB-OIB array, or on a vector at a steep angle to the array [140]. As Figure 16a shows, both the Limahe and Baixintan intrusions plot above the MORB-OIB array, indicating crustal contamination and a metasomatized mantle source of them, respectively. However, unlike the Limahe intrusion showing an affinity with the OIB components, the samples of Baixintan have lower Th/Yb ratio, which are closer to the E-MORB components. There is a similar case in the Nb/Yb -TiO_2/Yb diagram (Figure 16b), where the samples from the Limahe intrusion mostly plot in the OIB array due to its mantle plume source, while more than half of the samples from the Baixintan intrusion plot in the E-MORB field inside of the MORB array.

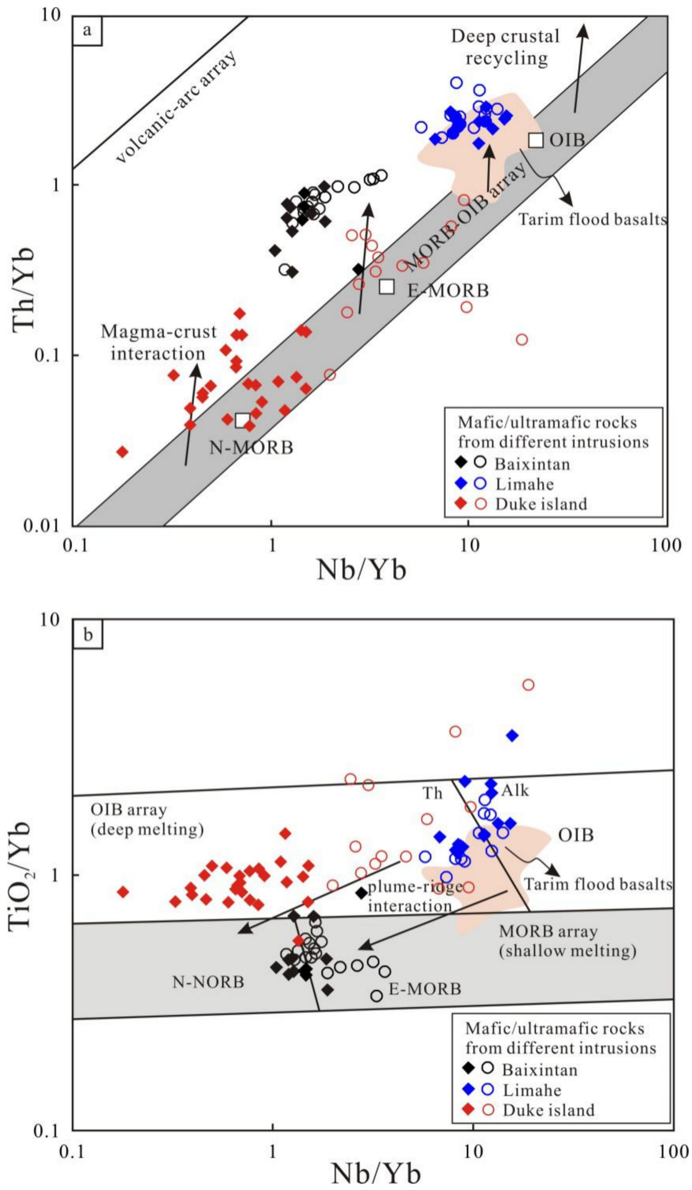

Figure 16. Nb/Yb-Th/Yb diagram (**a**) and Nb/Yb-TiO_2/Yb diagram (**b**) for the Baixintan, Limahe, and Duke Island intrusions (after [140]). Data sources are the same as in Figure 14.

It is generally believed that N-MORB and OIB are two separate end members, while E-MORB is mixed by N-MORB and OIB in different degrees [141–143], which is considered to be the result of plume and Mid-Ocean Ridge interaction [144–146]. It is suggested that E-MORB formed at plume-proximal ridge settings [140]. Similar geochemical characteristics of the Baixintan intrusion to those of E-MORB imply that it may be generated from a plume-related setting.

In consideration of geochronology and geochemical characteristics of the Baixintan intrusion, we suggest that the Baixintan intrusion may be generated from a back-arc spreading environment and related to a mantle plume.

6.3. Conceptional Genetic Model

Based on the nature of the magma source and the tectonic setting of the Baixintan intrusion reflected by geochemical characteristics, this paper proposes a geological evolutionary process for the Eastern Tianshan region: before the Early Permian, the subduction of the Paleo-Asian Ocean had altered the lithospheric mantle beneath the Eastern Tianshan region, making it contain some subduction slab-derived fluids' components. However, the subduction event did not impact the sources of intrusions located in the Beishan Rift on the south (Figure 17a). By the Early Permian, the Paleo-Asian Ocean had closed, and the Eastern Tianshan region was then in a back-arc spreading setting. By ~280 Ma, the mantle plume upwelled, and the magma derived from the mantle plume was influenced by lithospheric mantle containing subduction components. At last, the magma intruded into the crust, and ore-bearing mafic-ultramafic intrusions with the arc-like geochemical characteristics formed in the Eastern Tianshan orogenic belt (Figure 17b).

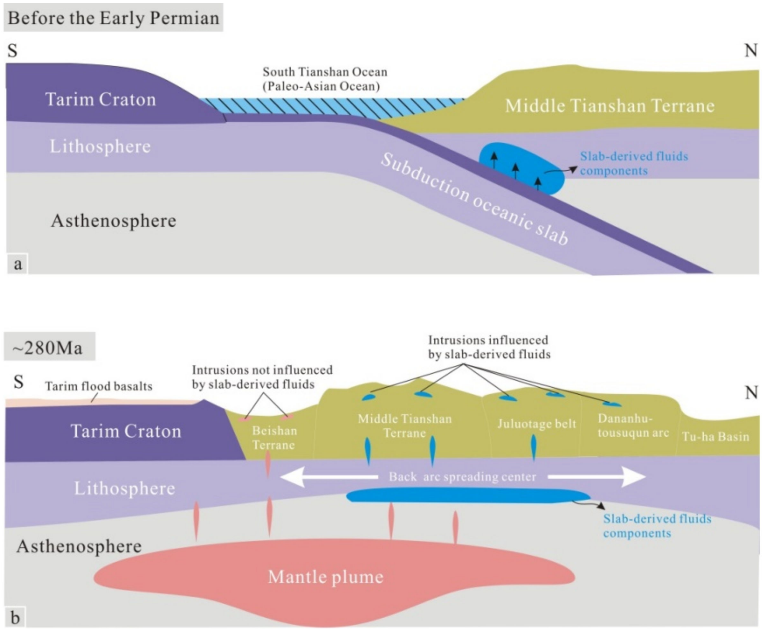

Figure 17. Proposed model showing (**a**) the evolution of the Paleo-Asian Ocean before the Early Permian, (**b**) mantle plume magmatism in the Eastern Tianshan region and the Beishan Rift in ~280 Ma.

7. Conclusions

The ~276 Ma Baixintan Ni-Cu ore-bearing mafic-ultramafic intrusion was emplaced in a back-arc spreading environment, and may be related to a mantle plume. The parental magmas for the Baixintan intrusion were likely high-Mg tholeiitic basaltic in composition and had already experienced sulfide segregation. The magma derived from the mantle plume was influenced by lithospheric mantle containing subduction slab-derived fluids' components, which give rise to the negative anomalies of Nb, Ta, and Ti elements in the Baixintan intrusion.

Supplementary Materials: The following are available online at https://www.mdpi.com/article/10.3390/min11040348/s1, Table S1. SHRIMP zircon U-Pb age data of sample BXT-B18 from the Baixintan intrusion.

Author Contributions: Conceptualization, M.Y. and W.L.; formal analysis, H.L.; investigation, M.Y. and X.L.; data curation, M.Y.; writing—original draft preparation, M.Y.; writing—review and editing, H.L. and Z.Z.; project administration, M.Y. All authors have read and agreed to the published version of the manuscript.

Funding: This research was funded by the Youth Program of National Science Foundation of China, grant number 41602094, 41603050.

Data Availability Statement: Data generated in this study is available in the article.

Acknowledgments: We are very grateful to the Editor and the reviewers for their great help in improving this manuscript and constructive opinions.

Conflicts of Interest: The authors declare no conflict of interest.

Appendix A

Table A1. Zircon SHRIMP U-Pb age results for the olivine gabbro from the Baixintan intrusion.

Measure Point	$^{206}Pb_c$ %	U ppm	Th ppm	$^{232}Th/^{238}U$	$^{206}Pb^*$ ppm	$^{206}Pb/^{238}U$ Age	$^{207}Pb/^{206}Pb$ Age	$^{208}Pb/^{232}Th$ Age	$^{207}Pb^*/^{206}Pb^*$	errors ±%	$^{207}Pb^*/^{235}U$	errors ±%	$^{206}Pb^*/^{238}U$	errors ±%
BXT-1	0.13	385	703	1.89	14.4	273.9 ± 2.0	267 ± 57	269.5 ± 3.5	0.0516	2.5	0.3087	2.6	0.04341	0.76
BXT-2	0.14	602	866	1.49	22.8	278.4 ± 1.9	286 ± 58	269.7 ± 3.3	0.0520	2.6	0.3164	2.6	0.04413	0.68
BXT-3	0.17	1005	1921	1.98	38.2	278.9 ± 1.7	218 ± 49	268.5 ± 2.6	0.0505	2.1	0.3079	2.2	0.04422	0.61
BXT-4	0.00	388	544	1.45	14.6	275.5 ± 2.0	300 ± 50	275.1 ± 3.7	0.0523	2.2	0.3151	2.3	0.04366	0.75
BXT-5	0.19	605	858	1.47	23.0	278.9 ± 1.8	108 ± 47	273.6 ± 3.2	0.04819	2.0	0.2938	2.1	0.04422	0.67
BXT-6	0.18	512	1004	2.03	19.3	276.5 ± 1.9	209 ± 52	268.0 ± 3.1	0.0503	2.2	0.3039	2.3	0.04382	0.72
BXT-7	0.06	1356	1241	0.95	51.6	279.1 ± 1.6	237 ± 28	270.2 ± 2.5	0.05091	1.2	0.3106	1.3	0.04425	0.57
BXT-8	0.14	485	860	1.83	18.5	280.2 ± 2.0	295 ± 46	274.7 ± 3.3	0.0522	2.0	0.3198	2.2	0.04442	0.72
BXT-9	0.08	593	1367	2.38	22.3	275.9 ± 1.9	230 ± 51	267.9 ± 3.0	0.0508	2.2	0.3061	2.3	0.04374	0.69
BXT-10	–	294	664	2.34	11.2	280.3 ± 2.3	311 ± 58	277.9 ± 3.9	0.0526	2.5	0.3221	2.7	0.04444	0.84
BXT-11	0.15	957	1513	1.63	36.5	279.2 ± 1.7	298 ± 34	272.8 ± 2.6	0.05228	1.5	0.3191	1.6	0.04427	0.61
BXT-12	0.21	685	1069	1.61	26.1	279.0 ± 1.8	104 ± 52	270.4 ± 3.0	0.0481	2.2	0.2933	2.3	0.04423	0.66
BXT-13	0.09	358	605	1.75	13.4	275.1 ± 2.1	263 ± 58	259.4 ± 4.7	0.0515	2.5	0.3096	2.6	0.04360	0.78
BXT-14	0.20	1090	2190	2.08	41.0	275.7 ± 1.6	211 ± 36	265.9 ± 2.4	0.05035	1.6	0.3033	1.7	0.04369	0.60
BXT-15	0.26	521	948	1.88	19.6	275.6 ± 1.9	190 ± 67	265.6 ± 3.3	0.0499	2.9	0.3005	3.0	0.04368	0.72
BXT-16	0.09	932	1326	1.47	34.8	274.0 ± 1.7	284 ± 35	269.6 ± 2.7	0.05196	1.5	0.3111	1.6	0.04342	0.62
BXT-17	0.10	1455	2062	1.46	54.9	276.9 ± 1.5	190 ± 29	268.5 ± 2.3	0.04990	1.3	0.3019	1.4	0.04388	0.57
BXT-18	0.15	540	909	1.74	20.1	272.4 ± 1.9	232 ± 50	269.2 ± 3.2	0.0508	2.2	0.3023	2.3	0.04315	0.70
BXT-19	0.05	1003	1658	1.71	37.3	273.3 ± 1.6	282 ± 33	264.5 ± 2.5	0.05192	1.4	0.3100	1.6	0.04331	0.62
BXT-20	0.20	1218	2709	2.30	45.8	275.6 ± 1.6	202 ± 31	270.4 ± 4.2	0.05015	1.3	0.3020	1.4	0.04368	0.59
BXT-21	0.26	750	1494	2.06	28.7	280.0±1.9	212±60	273.0 ± 3.1	0.0504	2.6	0.3082	2.7	0.04439	0.70

Errors are 1-sigma; Pb_c and Pb* indicate the common and radiogenic portions, respectively. Error in Standard calibration was 0.22% (not included in above errors but required when comparing data from different mounts). (1) Common Pb corrected using measured ^{204}Pb. (2) Common Pb corrected by assuming $^{206}Pb/^{238}U$-$^{207}Pb/^{235}U$ age-concordance. (3) Common Pb corrected by assuming $^{206}Pb/^{238}U$-$^{208}Pb/^{232}Th$ age-concordance.

Table A2. Major (wt. %) and trace element ($\times 10^{-6}$) analyses of the Baixintan intrusion.

Sample	BXT-B5	BXT-B10	BXT-B14	BXT-B17	BXT-B19	BXT-B20	BXT-B21	BXT-B22	BXT-B25	BXT-B26	GWB07104/ GWB07105	GWB07104/ GWB07105
Rock types	Lherzolite	Lherzolite	Lherzolite	Lherzolite	Lherzolite	Olivine Gabbro	Lherzolite	Gabbro	Gabbro	Gabbro	Andesite/ Basalt	Andesite/ Basalt
	Analytical Values											Recommended Values
SiO_2	41.33	40.75	41.10	41.25	42.72	47.87	42.22	45.27	47.96	48.42	60.71	60.62
TiO_2	0.31	0.30	0.35	0.38	0.42	0.59	0.48	0.49	1.33	0.57	0.521	0.515
Al_2O_3	5.84	5.02	5.36	5.74	7.54	18.04	4.39	15.32	16.98	17.62	16.12	16.17
TFeO	11.33	11.70	11.48	11.39	10.90	6.66	11.86	7.45	8.57	5.49	4.88	4.41
MnO	0.18	0.18	0.18	0.18	0.17	0.11	0.18	0.12	0.16	0.10	0.078	0.078
MgO	30.10	32.28	31.22	29.99	26.79	10.67	30.78	14.92	7.93	9.87	1.71	1.72
CaO	3.33	2.82	2.90	3.11	4.09	9.57	2.62	7.94	9.02	10.09	5.26	5.20
Na_2O	0.75	0.66	0.77	0.82	1.04	2.14	0.78	2.21	3.48	3.27	3.89	3.86
K_2O	0.29	0.22	0.29	0.32	0.34	0.37	0.41	0.25	0.43	0.29	1.87	1.89
P_2O_5	0.074	0.062	0.071	0.082	0.083	0.095	0.092	0.074	0.18	0.073	0.244	0.236
NiO	0.148	0.158	0.144	0.148	0.116	0.0308	0.138	0.0461	0.016	0.0226	0.0024	0.0021
Cr_2O_3	0.36	0.385	0.334	0.338	0.247	0.0587	0.328	0.0931	0.0294	0.077	0.0043	0.0046
LOI	5.50	5.03	5.32	5.76	5.11	3.54	5.24	5.58	3.64	3.87	4.44	4.44
$Mg^{\#}$	82.57	83.11	82.90	82.44	81.42	74.05	82.23	78.11	62.26	76.22	-	-
MgO/TFeO	2.66	2.76	2.72	2.63	2.46	2.60	2.11	2.00	1.80	1.60	-	-
Total	99.90	99.90	99.87	99.90	99.86	99.91	99.89	99.94	99.94	99.89	-	-
Rb	9.52	6.54	7.38	7.93	8.6	9.26	8.72	7.04	7.52	5.17	40.25	37
Sr	163	120	132	193	197	383	60.8	324	494	463	1192.2	1100
Ba	74	60.2	65.9	76	88	113	82.3	94.2	142	167	512.7	527
Y	10.40	6.50	7.00	7.87	8.63	12.80	10.20	10.20	15.20	13.40	21.95	22
Zr	30.7	27.1	28.6	31.1	35.1	46.1	45.7	35.4	70.1	46.6	271.50	277
Nb	3.05	2.6	2.43	2.27	2.1	2.13	2.18	1.68	4.33	1.94	70.21	68
Ta	0.37	0.33	0.39	0.33	0.35	0.34	0.34	0.30	0.40	0.25	4.127	4.3
Hf	0.97	0.81	0.91	0.98	1.12	1.46	1.40	1.16	1.82	1.38	6.463	6.5
Th	1.00	0.81	0.82	0.83	0.94	1.08	0.98	1.02	0.50	0.84	5.81	6.0

Table A3. Major (wt. %) and trace element ($\times 10^{-6}$) analyses of the Baixintan intrusion.

Sample	BXT-B5	BXT-B10	BXT-B14	BXT-B17	BXT-B19	BXT-B20	BXT-B21	BXT-B22	BXT-B25	BXT-B26	GWB07104/ GWB07105	GWB07104/ GWB07105
Rock types	Lherzolite	Lherzolite	Lherzolite	Lherzolite	Lherzolite	Olivine Gabbro	Lherzolite	Gabbro	Gabbro	Gabbro	Andesite/ Basalt	Andesite/ Basalt
	Analytical Values											Recommended Values
U	0.19	0.18	0.18	0.20	0.25	0.34	0.30	0.45	0.28	0.30	1.331	1.4
Pb	3.34	2.1	3.05	2.24	2.9	3.04	2.3	2.84	1.69	3.96	6.76	7
Cs	0.77	0.37	0.56	1.28	1.08	0.48	0.55	0.68	0.52	0.89	0.635	0.7
La	3.65	2.91	3.27	3.67	4.06	5.19	4.58	4.10	6.09	4.62	54.81	56
Ce	8.76	6.95	7.65	8.85	9.67	12.30	10.30	9.66	15.00	10.80	104.62	105
Pr	1.22	0.98	1.09	1.22	1.32	1.75	1.50	1.42	2.31	1.59	12.74	13.2
Nd	5.46	4.44	4.94	5.67	5.98	8.15	6.95	6.46	11.10	7.69	48.43	54
Sm	1.48	1.14	1.31	1.46	1.63	2.25	1.84	1.79	3.00	2.21	9.84	10.2
Eu	0.53	0.38	0.44	0.47	0.54	0.80	0.54	0.64	1.18	0.84	3.215	3.2
Gd	1.63	1.14	1.34	1.50	1.67	2.30	1.94	1.82	2.96	2.40	8.38	8.5
Tb	0.29	0.20	0.24	0.27	0.29	0.44	0.32	0.34	0.55	0.42	1.191	1.2
Dy	1.63	1.22	1.42	1.54	1.75	2.55	1.93	2.01	2.90	2.54	5.53	5.6
Ho	0.36	0.26	0.30	0.33	0.36	0.52	0.40	0.41	0.57	0.53	0.844	0.88
Er	0.96	0.72	0.81	0.90	1.01	1.46	1.16	1.13	1.62	1.40	1.958	2.0
Tm	0.15	0.11	0.12	0.14	0.15	0.22	0.18	0.18	0.24	0.21	0.261	0.28
Yb	0.92	0.72	0.77	0.86	0.96	1.45	1.16	1.14	1.56	1.35	1.437	1.5
Lu	0.14	0.11	0.12	0.13	0.15	0.23	0.18	0.18	0.23	0.20	0.172	0.19
∑REE	37.57	27.78	30.81	34.87	38.17	52.41	43.18	41.48	64.52	50.19	-	-
LREE	21.10	16.79	18.70	21.34	23.20	30.44	25.71	24.07	38.68	27.75	-	-
HREE	16.47	10.98	12.11	13.53	14.97	21.97	17.47	17.41	25.84	22.44	-	-
LREE/HREE	1.28	1.53	1.54	1.58	1.55	1.39	1.47	1.38	1.50	1.24	-	-
δEu	1.04	1.00	1.00	0.97	0.98	0.87	1.06	1.08	1.20	1.11	-	-

Note: $Mg^{\#} = 100 \times Mg^{2+}/(Mg^{2+} + Fe^{2+})$, $TFeO = FeO + 0.8998 \times Fe_2O_3$, and $\delta Eu = 2 \times Eu_N/(Sm_N + Gd_N)$.

Table A4. Sr-Nd isotopic analytical results of samples from the Baixintan intrusion.

Sample No.	BXT-B5	BXT-B10	BXT-B14	BXT-B17	BXT-B19	BXT-B20	BXT-B21	BXT-B22	BXT-B23	BXT-B25	BXT-B26
Rock Types	Lherzolite	Lherzolite	Lherzolite	Lherzolite	Lherzolite	Olivine Gabbro	Lherzolite	Gabbro	Lherzolite	Gabbro	Gabbro
Rb ($\times10^{-6}$)	11.34	7.11	8.06	9.58	9.76	8.73	10.78	6.96	4.77	10.10	5.87
Sr ($\times10^{-6}$)	175.76	127.38	133.10	206.04	201.95	393.46	56.91	386.14	225.34	516.02	468.92
$^{87}Rb/^{86}Sr$	0.186609	0.161571	0.175169	0.134506	0.139896	0.064176	0.548149	0.052160	0.061252	0.056626	0.036231
$^{87}Sr/^{86}Sr$	0.704373	0.704181	0.704230	0.704948	0.704319	0.703920	0.706009	0.704282	0.704570	0.703719	0.704097
2σ	0.000012	0.000010	0.000010	0.000010	0.000012	0.000011	0.000010	0.000010	0.000011	0.000013	0.000012
$(^{87}Sr/^{86}Sr)_i$	0.703638	0.703545	0.703540	0.704418	0.703768	0.703667	0.703850	0.704077	0.704329	0.703496	0.703954
Sm ($\times10^{-6}$)	1.21	1.07	1.23	1.31	1.47	2.12	1.67	1.70	1.33	2.99	2.16
Nd ($\times10^{-6}$)	4.88	4.06	4.66	5.08	5.61	7.69	6.25	6.05	4.86	11.06	7.24
$^{147}Sm/^{144}Nd$	0.150392	0.159137	0.159332	0.155910	0.157928	0.166553	0.160894	0.169709	0.164625	0.163339	0.179852
$^{143}Nd/^{144}Nd$	0.512794	0.512820	0.512801	0.512830	0.512842	0.512884	0.512826	0.512843	0.512849	0.512972	0.512870
2σ	0.000026	0.000020	0.000021	0.000016	0.000015	0.000013	0.000016	0.000018	0.000016	0.000008	0.000012
$(^{143}Nd/^{144}Nd)_i$	0.512522	0.512532	0.512512	0.512548	0.512556	0.512582	0.512534	0.512536	0.512551	0.512676	0.512544
εNd(t)	4.68	4.88	4.50	5.19	5.35	5.87	4.94	4.96	5.25	7.70	5.12
Age (Ma)						276.8					

Standards	Recommended value		Analytical value		Recommended value		Analytical value	
	$^{87}Sr/^{86}Sr$	2σ	$^{87}Sr/^{86}Sr$	2σ	$^{143}Nd/^{144}Nd$	2σ	$^{143}Nd/^{144}Nd$	2σ
BHVO-2	0.70348	0.0002	0.703484	0.00007	0.51297	0.00003	0.512950	0.000008
BCR-1	0.70501	0.0002	0.705017	0.00009	0.51263	0.00002	0.512641	0.000011

Table A5. Concentrations of chalcophile elements in the Baixintan intrusion.

Sample No.	BXT-B5	BXT-B10	BXT-B14	BXT-B17	BXT-B19	BXT-B20	BXT-B21	BXT-B22	BXT-B23	BXT-B25	BXT-B26
Rock Types	**Lherzolite**	**Lherzolite**	**Lherzolite**	**Lherzolite**	**Lherzolite**	**Olivine Gabbro**	**Lherzolite**	**Gabbro**	**Lherzolite**	**Gabbro**	**Gabbro**
Os	0.21	0.29	0.34	0.23	0.07	0.03	0.12	0.04	0.1	0.07	0.04
Ir	0.11	0.14	0.16	0.11	0.06	0.03	0.06	<0.02	<0.02	0.03	<0.02
Ru	0.32	0.34	0.41	0.32	0.19	0.17	0.22	0.15	0.17	0.15	0.16
Rh	0.11	0.12	0.16	0.12	0.06	0.03	0.06	0.03	0.42	0.02	0.23
Pt	1.58	2.43	2.73	1.72	0.69	0.2	1.59	0.2	0.24	0.24	<0.2
Pd	0.95	1.12	1.05	0.94	0.6	0.2	0.67	0.21	0.34	0.3	<0.2
Ni	1090	1300	1160	1170	949	201	1110	314	403	106	174
Cu	72.6	124	106	148	230	46.4	115	91.7	127	18.9	90.9
S	1338	1124	919	1147	2180	883	1030	507	408	638	547
ΣPGE	3.28	4.44	4.85	3.44	1.67	0.66	2.72	-	-	0.81	-
IPGE	0.64	0.77	0.91	0.66	0.32	0.23	0.40	-	-	0.25	-
PPGE	2.64	3.67	3.94	2.78	1.35	0.43	2.32	0.44	1.00	0.56	-
Ni/Cu	15.01	10.48	10.94	7.91	4.13	4.33	9.65	3.42	3.17	5.61	1.91
Pd/Ir	8.64	8.00	6.56	8.55	10.00	6.67	11.17	-	-	10.00	-
Cu/Pd	76.42	110.71	100.95	157.45	383.33	232.00	171.64	436.67	373.53	63.00	-

Sample	GBW07290 (Peridotite)		GBW07291 (Pyroxene peridotete)	
	Analytical results	Reference values	Analytical results	Reference values
Os	7.59	9.6 ± 2.0	1.99	2.4 ± 0.6
Ir	4.07	4.3 ± 0.5	6.45	4.7 ± 1.1
Ru	10.0	14.7 ± 2.7	1.80	2.5 ± 0.2
Rh	1.23	1.3 ± 0.3	5.05	4.3 ± 0.8
Pt	6.39	6.4 ± 0.9	62.8	58 ± 5
Pd	3.83	4.6 ± 0.6	73.9	60 ± 9

Sample	GXR-1		GXR-3	
	Analytical results	Recommended values	Analytical results	Recommended values
Ni	44.2	41	65.1	60
Cu	1055	1110	17.2	15
S	2657	2570	2428	2320

Ni, Cu, S in ppm, PGEs in ppb.

References

1. Qin, K.Z.; Fang, T.H.; Wang, S.L.; Zhu, B.Q.; Feng, Y.M.; Yu, H.F.; Xiu, Q.Y. Plate tectonic division, evolution and metallogenic settings in Eastern Tianshan Mountains, NW-China. *Xinjiang Geol.* **2002**, *20*, 302–308. (In Chinese with English abstract)
2. Han, B.F.; Ji, J.Q.; Song, B.; Chen, L.H.; Li, Z.H. SHRIMP zircon U-Pb ages of the Kalatongke and the Huangshandong ore-bearing mafic-ultramafic intrusions and the geological significance. *Chin. Sci. Bull.* **2004**, *49*, 2325–2328. (In Chinese)
3. Zhou, M.F.; Lesher, C.M.; Yang, Z.X.; Li, J.W.; Sun, M. Geochemistry and petrogenesis of 270 Ma Ni-Cu-(PGE) sulfide-bearing mafic intrusions in the Huangshan district, Eastern Xinjiang, Northwest China: Implications for the tectonic evolution of the Central Asian orogenic belt. *Chem. Geol.* **2004**, *209*, 233–257. [CrossRef]
4. Wu, H.; Li, H.Q.; Mo, X.H.; Chen, F.W.; Lu, Y.F.; Mei, Y.P.; Deng, G. Age of the Baishiquan mafic-ultramafic complex, Hami, Xinjiang and its geological significance. *Acta Geol. Sin.* **2005**, *79*, 498–502. (In Chinese with English abstract)
5. Mao, Q.G.; Xiao, W.J.; Han, C.M.; Sun, M.; Yuan, C.; Yan, Z.; Li, J.L.; Yong, Y.; Zhang, J.E. Zircon U-Pb age and the geochemistry of the Baishiquan mafic-ultramafic complex in the Eastern Tianshan, Xinjiang province: Constrains on the closure of the Paleo-Asian Ocean. *Acta Petrol. Sin.* **2006**, *22*, 153–162. (In Chinese with English abstract)
6. Xia, M.Z.; Jiang, C.Y.; Qian, Z.Z.; Sun, T.; Xia, Z.D.; Lu, R.H. Geochemistry and petrogenesis for Hulu intrusion in East Tianshan, Xinjiang. *Acta Petrol. Sin.* **2008**, *24*, 2749–2760. (In Chinese with English abstract)
7. Tang, D.M.; Qin, K.Z.; Sun, H.; Su, B.X.; Xiao, Q.H.; Cheng, S.L.; Li, J. Lithological, chronological and geochemical characteristics of Tianyu Cu-Ni deposit: Constrains on source and genesis of mafic-ultramafic intrusions in eastern Xinjiang. *Acta Petrol. Sin.* **2009**, *25*, 817–831. (In Chinese with English abstract)
8. San, J.Z.; Qin, K.Z.; Tang, Z.L.; Tang, D.M.; Su, B.X.; Sun, H.; Xiao, Q.H.; Liu, P.P. Precise zircon U-Pb age dating of two mafic-ultramafic complexes at Tulaergen large Cu-Ni district and its geological implications. *Acta Petrol. Sin.* **2010**, *26*, 3027–3035. (In Chinese with English abstract)
9. Chen, J.P.; Luo, T.; Wang, H.; Liao, Q.A.; Zhang, X.H.; Chen, E.K.; Wang, J.J.; Meng, Q.Y.; Liu, X.M. Zircon Hf isotope characteristics and source of mafic-ultramafic intrusions in Huangshan region, Xinjiang. *Northwestern Geol.* **2016**, *49*, 51–61. (In Chinese with English abstract)
10. Feng, Y.Q.; Qian, Z.Z.; Duan, J.; Xu, G.; Ren, M.; Jiang, C. Geochronological and geochemical study of the Baixintan magmatic Ni-Cu sulphide deposit: New implications for the exploration potential in the western part of the East Tianshan nickel belt (NW China). *Ore Geol. Rev.* **2018**, *95*, 366–381. [CrossRef]
11. Sun, T.; Qian, Z.Z.; Tang, Z.L.; Jiao, J.G.; He, K.; Zhao, X.J.; Zhang, R. Process of magmatic mineralization of Cu-Ni Sulfide deposits in the Eastern Tianshan area. *Acta Mineral. Sin.* **2011**, *S1*, 170–171. (In Chinese)
12. Deng, Y.F.; Song, X.Y.; Xie, W.; Cheng, S.L.; Li, J. Petrogenesis of the Huangshandong Ni-Cu sulfide-bearing mafic-ultramafic intrusion, Northern Tianshan, Xinjiang: Evidence from major and trace elements and Sr-Nd isotope. *Acta Geol. Sin.* **2011**, *85*, 1435–1451. (In Chinese with English abstract)
13. Jiao, J.G.; Tang, Z.L.; Qian, Z.Z.; Sun, T.; Duan, J.; Jiang, C. Genesis and metallogenic process of Tulaergen large scale Cu-Ni deposit in eastern Tianshan area, Xinjiang. *Acta Petrol. Sin.* **2012**, *28*, 3772–3786. (In Chinese with English abstract)
14. Gao, J.F.; Zhou, M.F.; Lightfoot, P.C.; Wang, C.Y.; Qi, L.; Sun, M. Sulfide saturation and magma emplacement in the formation of the Permian Huangshandong Ni-Cu sulfide deposit, Xinjiang, Northwestern China. *Econ. Geol.* **2013**, *108*, 1833–1848. [CrossRef]
15. Mao, Y.J.; Qin, K.Z.; Tang, D.M.; Feng, H.Y.; Xue, S.C. Crustal contamination and sulfide immiscibility history of the Permian Huangshannan magmatic Ni-Cu sulfide deposit, East Tianshan, NW China. *J. Asian Earth Sci.* **2016**, *129*, 22–37. [CrossRef]
16. You, M.X.; Zhang, Z.W.; Wang, Y.L.; Qian, B.; Zhang, J.W. Zircon U-Pb age and the magma evolution process of the Huangshannan mafic-ultramafic intrusion in the East Tianshan mountains. *Geol. Explor.* **2017**, *53*, 903–914. (In Chinese with English abstract)
17. You, M.X.; Li, H.M.; Wang, Y.L. Magma evolution of Huangshannan mafic-ultramafic intrusion in East Tianshan region: Indication from mineralogy and Sr, Nd isotopic characteristics. *Acta Petrologica Sinica* **2018**, *34*, 3422–3432. (In Chinese with English abstract)
18. Qin, K.Z.; Zhai, M.G.; Li, G.M.; Zhao, J.X.; Zeng, Q.D.; Gao, J.; Xiao, W.J.; Li, J.L.; Sun, S. Links of collage orogenesis of multiblocks and crust evolution to characteristic metallogenesis in China. *Acta Petrol. Sin.* **2017**, *33*, 305–325. (In Chinese with English abstract)
19. Zhang, Z.H.; Chai, F.M.; Du, A.D.; Zhang, Z.C.; Yan, S.H.; Yang, J.M.; Qu, W.J.; Wang, Z.L. Re-Os dating and ore-forming material tracing of the Kalatongke Cu-Ni sulfide deposit in northern Xinjiang. *Acta Petrol. Et Mineral.* **2005**, *24*, 285–293. (In Chinese with English abstract)
20. Gu, L.X.; Zhang, Z.Z.; Wu, C.Z.; Tang, J.H.; San, J.Z.; Wang, C.S.; Zhang, G.H. Permian geological, metallurgical and geothermal events of the Huangshan-Jing'erquan area, eastern Tianshan: Indications for mantle magma intraplating and its effect on the crust. *Acta Petrol. Sin.* **2007**, *23*, 2869–2880. (In Chinese with English abstract)
21. Wang, J.B.; Wang, Y.W.; Zhou, T.F. Metallogenic spectrum related to post-collisional mantle-derived magma in north Xinjiang. *Acta Petrol. Sin.* **2008**, *24*, 743–752. (In Chinese with English abstract)
22. Zhou, M.F.; Zhao, J.H.; Jiang, C.Y.; Gao, J.F.; Wang, W.; Yang, S.H. OIB-like heterogeneous mantle sources of Permian basaltic magmatism in the western Tarim Basin, NW China: Implications for a possible Permian large igneous province. *Lithos* **2009**, *113*, 583–594. [CrossRef]
23. Mao, J.W.; Pirajno, F.; Zhang., Z.H.; Chai, F.M.; Yang, J.M.; Wu, H.; Chen, S.P.; Cheng, S.L.; Zhang, C.Q. Late Variscan post-collisional Cu-Ni sulfide deposits in East Tianshan and Altay in China principal characteristics and the possible relationship with mantle plume. *Acta Geol. Sin.* **2006**, *80*, 925–942. (In Chinese with English abstract)

24. Mao, J.W.; Pirajno, F.; Zhang. Z., H.; Chai, F.M.; Wu, H.; Chen, S.P.; Chen, L.S.; Yang, J.M.; Zhang, C.Q. A review of the Cu-Ni sulphide deposits in the Chinese Tianshan and Altay orogens (Xinjiang Autonomous Region, NW China): Principal characteristics and ore-forming processes. *J. Asian Earth Sci.* **2008**, *32*, 184–203. [CrossRef]
25. Pirajno, F.; Mao, J.W.; Zhang, Z.C.; Zhang, Z.H.; Chai, F.M. The association of mafic-ultramafic intrusions and A-type magmatism in the Tian Shan and Altay orogens, NW China: Implications for geodynamic evolution and potential for the discovery of new ore deposits. *J. Asian Earth Sci.* **2008**, *32*, 165–183. [CrossRef]
26. Xu, Y.G.; He, B.; Luo, Z.Y.; Liu, H.Q. Study on mantle plume and large igneous provinces in China: An overview and perspectives. *Bull. Mineral. Petrol. Geochem.* **2013**, *32*, 25–39. (In Chinese with English abstract)
27. Liu, Y.G.; Lü, X.B.; Wu, C.M.; Hu, X.G.; Duan, Z.P.; Deng, G.; Wang, H.; Zhu, X.; Zeng, H.D.; Wang, P.; et al. The migration of Tarim plume magma toward the northeast in Early Permian and its significance for the exploration of PGE-Cu-Ni magmatic sulfide deposits in Xinjiang, NW China: As suggested by Sr-Nd-Hf isotopes, sedimentology and geophysical data. *Ore Geol. Rev.* **2016**, *72*, 538–545. [CrossRef]
28. Qin, K.Z.; Su, B.X.; Sakyi, P.A.; Tang, D.M.; Li, X.H.; Sun, H.; Xiao, Q.H.; Liu, P.P. SIMS zircon U-Pb geochronology and Sr-Nd isotopes of Ni-Cu-bearing mafic-ultramafic intrusions in eastern Tianshan and Beishan in correlation with flood basalts in Tarim basin (NW China): Constraints on a ca. 280Ma mantle plume. *Am. J. Sci.* **2011**, *311*, 237–260. [CrossRef]
29. Su, B.X.; Qin, K.Z.; Sakyi, P.A.; Li, X.H.; Yang, Y.H.; Sun, H.; Tang, D.M.; Liu, P.P.; Xiao, Q.H.; Malaviarachchi, S.P.K. U-Pb ages and Hf-O isotopes of zircons from Late Paleozoic mafic-ultramafic units in the southern Central Asian Orogenic Belt: Tectonic implications and evidence for an Early-Permain mantle plume. *Gondwana Res.* **2011**, *20*, 516–531. [CrossRef]
30. Su, B.X.; Qin, K.Z.; Santosh, M.; Tang, D.M. The Early Permian mafic-ultramafic complexes in the Beishan Terrane, NW China: Alaskan-type intrusives or rift cumulates? *J. Asian Earth Sci.* **2013**, *66*, 175–187. [CrossRef]
31. Su, B.X.; Qin, K.Z.; Zhou, M.F.; Sakyi, P.A.; Thakurta, J.; Tang, D.M.; Liu, P.P.; Xiao, Q.H.; Sun, H. Petrological, geochemical and geochronological constraints on the origin of the Xiadong Ural-Alaskan type complex in NW China and tectonic implication for the evolution of southern Central Asian Orogenic Belt. *Lithos* **2014**, *200*, 226–240. [CrossRef]
32. Li, W.Y.; Niu, Y.L.; Zhang, Z.W.; Zhang, M.J.; Gao, Y.B.; Hu, P.Q.; Zhang, J.W.; Tan, W.J.; Jiang, H.B. Geodynamic setting and further exploration of magmatism-related mineralization concentrated in the late Paleozoic in the northern Xinjiang Autonomous Region. *Earth Sci. Front.* **2012**, *19*, 41–50. (In Chinese with English abstract)
33. Li, W.Y. The primary discussion on the relationship between Paleo-Asian Ocean and Paleo-Tethys Ocean. *Acta Petrol. Sin.* **2018**, *34*, 2201–2210. (In Chinese with English abstract)
34. Xiao, W.J.; Zhang, L.C.; Qin, Z.; Sun, S.; Li, J.L. Paleozoic accretionary and collisional tectonics of the Eastern Tianshan (China): Implications for the continental growth of central Asia. *Am. J. Sci.* **2004**, *304*, 370–395. [CrossRef]
35. Xiao, W.J.; Han, C.M.; Yuan, C.; Chen, H.L.; Sun, M.; Lin, S.F.; Li, Z.L.; Mao, Q.G.; Zhang, J.E.; Sun, S.; et al. Unique Carboniferous-Permian tectonic-metallogenic framework of Northern Xinjiang (NW China): Constraints for the tectonics of the southern Paleo Asian Domain. *Acta Petrol. Sin.* **2006**, *22*, 1062–1076. (In Chinese with English abstract)
36. Su, B.X.; Qin, K.Z.; Sakyi, P.A.; Malaviarachchi, S.P.K.; Liu, P.P.; Tang, D.M.; Xiao, Q.H.; Sun, H.; Ma, Y.G.; Mao, Q. Occurrence of an Alaskan-type complex in the Middle Tianshan Massif, Central Asian Orogenic Belt: Inferences from petrological and mineralogical studies. *Int. Geol. Rev.* **2012**, *54*, 249–269. [CrossRef]
37. Wang, Z.X.; Wu, J.Y.; Liu, C.D.; Lv, X.C.; Zhang, J.G. *Multicycle Tectonic Evolution and Mineralization in Tianshan Mountains*; Science Press: Beijing, China, 1990; pp. 29–37.
38. Windley, B.F.; Allen, M.B.; Zhang, C.; Zhao, Z.Y.; Wang, G.R. Paleozoic accretion and Cenozoic redeformation of the Chinese Tien Shan Range Central Asia. *Geology* **1990**, *18*, 128–131. [CrossRef]
39. Allen, M.B.; Windley, B.F.; Zhang, C. Paleozoic collisional tectonics and magmatism of the Chinese Tien Shan, central Asia. *Tectonophysics* **1993**, *220*, 89–115. [CrossRef]
40. Gao, J.; Li, M.S.; Xiao, X.C.; Tang, Y.Q.; He, G.Q. Paleozoic tectonic evolution of the Tianshan Orogen, northwestern China. *Tectonophysics* **1998**, *287*, 213–231. [CrossRef]
41. Xia, L.Q.; Xu, X.Y.; Xia, Z.C.; Li, X.M.; Ma, Z.P.; Wang, L.S. Petrogenesis of carboniferous rift-related volcanic rocks in the Tianshan, northwestern China. *Geol. Soc. Am. Bull.* **2004**, *116*, 419–433. [CrossRef]
42. Gao, C.L.; Cui, K.R.; Qian, Y.X.; Liu, B.; Ding, D.G.; Ying, Y. *Tianshan Microplate Tectonics and Tabei Basin*; Geological Publishing House: Beijing, China, 1995; pp. 1–265. (In Chinese)
43. Lu, H.F.; Jia, D.; Cai, D.S.; Wu, S.M.; Chen, C.M.; Shi, Y.S. *Paleozoic Tectonic Evolution in Tarim River, Western Tianshan*; Science Press: Beijing, China, 1996; pp. 235–245. (In Chinese)
44. Hao, J.; Liu, X.H. Ophiolite mélange time and tectonic model in south Tianshan area. *Sci. Geol. Sin.* **1993**, *28*, 93–95. (In Chinese with English abstract)
45. Chen, X.J. The study of Paleozoic tectono-magmatism and geodynamic evolution in Eastern Tianshan, Northwest China. Ph.D. Thesis, Nanjing University, Nanjing, China, 2013.
46. Li, X.; Wang, D.K.; Zhao, S.M. The discovery of Baixintan magmatic Ni-Cu sulfide deposits in Hami area, Xinjiang. *Xinjiang Geol.* **2014**, *32*, 466–469. (In Chinese with English abstract)
47. Chai, F.M.; Zhang, Z.C.; Mao, J.W.; Dong, L.H.; Zhang, Z.H.; Wu, H. Geology, petrology and geochemistry of the Baishiquan Ni-Cu-bearing mafic-ultramafic intrusions in Xinjiang, NW China: Implications for tectonics and genesis of ores. *J. Asian Earth Sci.* **2008**, *32*, 218–235. [CrossRef]

48. Liu, Y.G.; Lü, X.B.; Yang, L.S.; Wang, H.F.; Meng, Y.F.; Yi, Q.; Zhang, B.; Wu, J.L.; Ma, J. Metallogeny of the Poyi magmatic Cu-Ni deposit: Revelation from the contrast of PGE and olivine composition with other Cu-Ni sulfide deposits in the Early Permian, Xinjiang, China. *Geosci. J.* **2015**, *19*, 613–620. [CrossRef]
49. Liu, Y.G.; Li, W.Y.; Lü, X.B.; Huo, Y.H.; Zhang, B. The Pobei Cu-Ni and Fe ore deposits in NW China are comagmatic evolution products: Evidence from ore microscopy, zircon U-Pb chronology and geochemistry. *Geol. Acta* **2017**, *15*, 37–50.
50. Liu, Y.G.; Li, W.Y.; Lü, X.B.; Liu, Y.R.; Ruan, B.X.; Liu, X. Sulfide saturation mechanism of the Poyi magmatic Cu-Ni sulfide deposit in Beishan, Xinjiang, Northwest China. *Ore Geol. Rev.* **2017**, *91*, 419–431. [CrossRef]
51. Liu, Y.G.; Lü, X.B.; Ruan, B.X.; Liu, X.; Liu, S.; Feng, J.; Deng, G.; Wang, H.; Zeng, H.D.; Wang, P.; et al. A comprehensive information exploration model for magmatic Cu-Ni sulfide deposits in Beishan, Xinjiang. *Miner. Depos.* **2019**, *38*, 644–666. (In Chinese with English abstract)
52. Li, J.Y. Late Neoproterozoic and Paleozoic tectonic framework and evolution of Eastern Xinjiang, NW China. *Geol. Rev.* **2004**, *50*, 304–322. (In Chinese with English abstract)
53. Wang, Y.F.; Chen, H.Y.; Han, J.S.; Chen, S.B.; Huang, B.Q.; Li, C.; Tian, Q.L.; Wang, C.; Wu, J.X.; Chen, M.X. Paleozoic tectonic evolution of the Dananhu-Tousuquan island arc belt, Eastern Tianshan: Constraints from the magmatism of the Yuhai porphyry Cu deposit, Xinjiang, NW China. *J. Asian Earth Sci.* **2017**, *153*, 282–306. [CrossRef]
54. Zhang, H.R.; Wei, G.Z.; Li, Y.J.; Du, Z.G.; Chai, D.L. Carboniferous lithologic association and tectonic evolution of Dananhu arc in the East Tianshan Mountains. *Acta Petrol. Et Mineral.* **2010**, *29*, 1–14.
55. Song, B.; Li, J.Y.; Li, W.Q.; Wang, K.Z.; Wang, Y. Shrimp dating of zircons from Dananhu and Kezirkalasayi granitoid batholith in southern margin of Tuha Basin and their geological implication. *Xinjiang Geol.* **2002**, *20*, 342–345. (In Chinese with English abstract)
56. Gu, L.X.; Zhang, Z.Z.; Wu, C.Z.; Wang, Y.X.; Tang, J.H.; Wang, C.S.; Xi, A.H.; Zheng, Y.Z. Some problems on granites and vertical growth of the continental crust in the eastern Tianshan Mountains, NW China. *Acta Petrol. Sin.* **2006**, *22*, 1103–1120. (In Chinese with English abstract)
57. Li, J.Y.; Song, B.; Wang, K.Z.; Li, Y.P.; Sun, G.H.; Qi, D.Y. Permian mafic-ultramafic complexes on the Southern margin of the Tu-Ha Basin, East Tianshan Mountains: Geological records of vertical growth in central Asia. *Acta Geosci. Sin.* **2006**, *27*, 424–446. (In Chinese with English abstract)
58. Pang, B.C.; Li, Q.G.; Chen, J.L.; Liu, S.W.; Wang, Z.Q.; Chen, Y.J.; Xiao, B. Paleozoic intrusive magmatic activity and basement properties of the Dannanhu-Tousuquan island arc in the Eastern Tianshan Mountains. *Northwestern Geol.* **2020**, *53*, 1–26. (In Chinese with English abstract)
59. Wang, J.B.; Wang, Y.W.; He, Z.J. Ore deposits as a guide to the tectonic evolution in the East Tianshan Mountains, NW China. *Geol. China* **2006**, *33*, 461–469. (In Chinese with English abstract)
60. Mao, Y.J.; Qin, K.Z.; Tang, D.M.; Xue, S.C.; Feng, H.Y.; Tian, Y. Multiple stages of magma emplacement and mineralization of eastern Tianshan, Xinjiang: Exemplified by the Huangshan Ni-Cu deposit. *Acta Petrol. Sin.* **2014**, *30*, 1575–1594. (In Chinese with English abstract)
61. Jahn, B.M. The Central Asian Orogenic Belt and growth of the continental crust in the Phanerozoic. *Asp. Tecton. Evol. China* **2004**, *226*, 73–100. [CrossRef]
62. Bureau of Geology and Mineral Resources of Xinjiang Uygur Autonomous Region (BGMRXUAR). *Regional Geology of Xinjiang Uygur Autonomous Region*; Geological Publishing House: Beijing, China, 1993; p. 841. (In Chinese)
63. Cao, R.; Muhetage, Z.R.; Wang, D.K.; Cao, F.Y. Structural Characteristics and plate boundary properties of the Kangguertage fault zone in Jueluotage orogenic belt, Eastern Tianshan. *Northwestern Geol.* **2016**, *49*, 28–38. (In Chinese with English abstract)
64. Geological Research Academy of Xinjiang (GRAX). *1:250,000 Report of Regional Geological Survey*; Geological Research Academy of Xinjiang (GRAX): Urumqi, China, 2003; p. 186. (In Chinese)
65. No. 1 Regional Geologcal Survey Party of Xinjiang Geology and Mineral Development Center (NRGSPXGMDC). The exploration report of the Baixintan Cu-Ni deposit. Xinjiang Institute of Ecology and Geography: Urumqi, China, 2014.
66. Williams, I.S. U-Th-Pb geochronology by ion microprobe. In *Reviews in Economic Geology, Applications of Microanalytical Techniques to Understanding Mineralizing Processes*; Mckibben, M.A., Shanks, W.C., Ridley, W.I., Eds.; Society of Economic Geologists: Littleton, CO, USA, 1998; Volume 7, pp. 1–35.
67. Song, B.; Zhang, Y.H.; Liu, D.Y. Introduction to the Naissance of SHRIMP and its contribution to isotope geology. *J. Chin. Mass Spectrom. Soc.* **2002**, *23*, 58–63. (In Chinese with English abstract)
68. Nasdala, L.; Hofmeister, W.; Norberg, N.; Mattinson, J.M.; Corfu, F.; Dorr, W.; Kamo, S.L.; Kennedy, A.K.; Kronz, A.; Reiners, P.W.; et al. Zircon M257—A homogeneous natural reference material for the lon microprobe U-Pb analysis of zircon. *Geostand. Geoanalytical Res.* **2008**, *32*, 247–265. [CrossRef]
69. Black, L.P.; Kamo, S.L.; Allen, C.M.; Aleinikoff, J.N.; Davis, D.W.; Korsch, R.J.; Foudoulis, C. TEMORA 1 a new zircon standard for Phanerozoic U-Pb geochronology. *Chemcal Geol.* **2003**, *200*, 155–170. [CrossRef]
70. Stacey, J.S.; Kramers, J.D. Approximation of terrestrial lead isotope evolution by a two-stage model. *Earth Planet. Sci. Lett.* **1975**, *26*, 207–221. [CrossRef]
71. Ludwig, K.R. *SQUID 1.03: A User's Manual. Berkeley Geochronology Center Special Publication No. 2*; Berkeley Geochronology Center: Berkeley, CA, USA, 2001; pp. 1–19.
72. Ludwig, K.R. *User's Manual for Isoplot 3.75, a Geochronological Toolkit for Microsoft Excel*; Berkeley Geochronology Center Special Publication No. 5; Berkeley Geochronology Center: Berkeley, CA, USA, 2012; pp. 25–32.

73. Institute of Geophysical and Geochemical Exporation, Chinese Academy of Geological Sciences. *Certified Reference Materials for the Chemical Composition of Rocks*; Institute of Geophysical and Geochemical Exporation, Chinese Academy of Geological Sciences: Beijing, China, 2012; pp. 1–4. (In Chinese)
74. Yang, J.D.; Tao, X.C.; Xue, Y.S. Nd isotopic variations of Chinese seawater during Neoproterozoic through Cambrian. *Chem. Geol.* **1997**, *135*, 127–137.
75. Gouveia, M.A.; Prudêncio, M.I.; Barros, J.S.; Morgado, L.; Cabral, J.M.P. Elemental concentration data for USGS Geochemical Exploration Reference Materials GXR-1 to GXR-4 and GXR-6. *J. Radioanal. Nucl. Chem.* **1994**, *179*, 165–172. [CrossRef]
76. He, H.L.; Lü, C.F.; Zhou, Z.R.; Shi, S.Y.; Li, B. Determination of platinum group elements and gold in geochemical exploration samples by nickel sulphide fire assay-ICPMS I. Simplification of the Analytical procedure. *Rock Miner. Anal.* **2001**, *20*, 191–194. (In Chinese with English abstract)
77. Lü, C.F.; He, H.L.; Zhou, Z.R.; Zhi, X.X.; Li, B.; Zhang, Q. Geochemical expolration samples by nickel sulfide fire assay-ICPMS II. Reduction of Reagent Blank. *Rock Miner. Anal.* **2002**, *21*, 7–11. (In Chinese with English abstract)
78. Corfu, F.; Hanchar, J.M.; Hoskin, P.W.; Kinny, P. Atlas of zircon textures. *Rev. Mineral. Geochem.* **2003**, *53*, 469–500. [CrossRef]
79. Hoskin, P.W.; Schaltegger, U. The composition of zircon and igneous and metamorphic petrogenesis. *Rev. Mineral. Geochem.* **2003**, *53*, 27–62. [CrossRef]
80. Tao, Y.; Hu, R.Z.; Qi, L.; Luo, T.Y. Geochemical characteristics and metallogenesis of the Limahe mafic-ultramafic intrusion, Sichuan. *Acta Petrol. Sin.* **2007**, *23*, 2785–2800. (In Chinese with English abstract)
81. Zhang, Z.C.; Li, Y.; Zhao, L.; Ai, Y. Geochemistry of three layered mafic-ultramafic intrusions in the Panxi area and constrains on their sources. *Acta Petrol. Sin.* **2007**, *23*, 2339–2352. (In Chinese with English abstract)
82. Sun, S.S.; McDonough, W.F. Chemical and isotopic systematics of oceanic basalts: Implications for mantle composition and processes. *Geol. Soc. Lond. Spec. Publ.* **1989**, *42*, 313–345. [CrossRef]
83. Zindler, A.; Hart, S.R. Chemical geodynamics. *Annu. Rev. Earth Planet. Sci.* **1986**, *14*, 493–571. [CrossRef]
84. Zhao, B.B.; Deng, Y.F.; Zhou, T.F.; Yuan, F.; Zhang, D.Y.; Deng, G.; Li, W.D.; Li, Y. Petrogenesis of the Baixintan Ni-Cu sulfide-bearing mafic-ultramafic intrusion, East Tianshan: Evidence from geochronology, petrogeochemistry and Sr-Nd isotope. *Acta Petrol. Sin.* **2018**, *34*, 2733–2753. (In Chinese with English abstract)
85. Wang, Y.L.; Zhang, Z.W.; Zhang, J.W.; You, M.X.; Li, K.; Wang, B.L. Mineralogy and Sr-Nd isotope characteristics of Baixintan Ni-Cu deposit in Eastern Tianshan Mountains, Xinjiang, and mineralization process. *Acta Geol. Sin.* **2016**, *90*, 2747–2758. (In Chinese with English abstract)
86. Feng, Y.Q.; Qian, Z.Z.; Duan, J.; Sun, T.; Xu, G.; Jiang, C.; Ren, M.; Chen, H.J. Genesis and ore-forming potential of mafic-ultramafic intrusions in the western part of East Tianshan Cu-Ni metallogenic belt, Xinjiang. *Acta Geol. Sin.* **2017**, *91*, 792–811.
87. Zhou, M.F.; Arndt, N.T.; Malpas, J.; Wang, C.Y.; Kennedy, A.K. Two magma series and associated ore deposit types in the Permian Emeishan large igneous province, SW China. *Lithos* **2008**, *103*, 352–368. [CrossRef]
88. Jiang, C.Y.; Zhang, P.B.; Lu, D.R.; Bai, K.Y.; Wang, Y.P.; Tang, S.H.; Wang, J.H.; Yang, C. Petrology, geochemistry and petrogenesis of the Kalpin basalts and their Nd, Sr and Pb isotopic compositions. *Geol. Rev.* **2004**, *50*, 492–500. (In Chinese with English abstract)
89. Yu, X. Magma evolution and deep geological process of Early Permian Tarim Large Igneous Province. Ph.D. Thesis, Zhejiang University, Hangzhou, China, 2009. (In Chinese with English abstract).
90. Wang, Z.C. Study of the petrogenesis of Tarim Permian Flood basalts, NW China. Master's Thesis, China University of Geosciences, Beijing, China, 2019. (In Chinese with English abstract).
91. McDonough, W.F.; Sun, S.S. The composition of the Earth. *Chem.Geol.* **1995**, *120*, 223–253. [CrossRef]
92. Kuno, H. *Differetiation of Basalt Magma*; Hess, H.H., Poldervaart, A., Eds.; John Wiley and Sons: New York, NY, USA, 1968; pp. 623–688.
93. Barnes, S.J.; Boyd, R.; Korneliussen, A.; Nilsson, L.P.; Often, M.; Penersen, R.B.; Robins, B. The use of mantle normalization and metal ratios in discriminating between the effects of partial melting, crystal fractionation and sulphide segregation on platinum-group elements, gold, nickel and copper: Examples from Norway. In *Geo-Platininum 87*; Springer: Dordrecht, Netherlands, 1988.
94. Li, P.; Zhao, T.Y.; Mi, B.X.; Han, Q. Platinum-group elements geochemistry and its significances of Baixintan Cu-Ni sulfide deposit in Eastern Tianshan, NW China. *Xinjiang Geol.* **2019**, *37*, 464–468. (In Chinese with English abstract)
95. Naldrett, A.J. World-class Ni-Cu-PGE deposits: Key factors in their genesis. *Miner. Depos.* **1999**, *34*, 227–240. [CrossRef]
96. Guan, J.X.; Song. X., Y. Platinum-group elements as ore potentiality tracer of a few small mafic-ultramafic intrusions in Panxi area, Sichuan Province. *Miner. Depos.* **2010**, *29*, 207–217. (In Chinese with English abstract)
97. Puchtel, I.S.; Humayun, M. Platinum group element fractionation in a komatiitic basalt lava lake. *Geochim. Et Cosmochim. Acta* **2001**, *65*, 2979–2993. [CrossRef]
98. Capobianco, C.J.; Hervig, R.L.; Drake, M.J. Experiments on crystal liquid partitioning of Ru, Rh, and Pd for magnetite and hematite solid-solutions crystallized from silicate melt. *Chem. Geol.* **1994**, *113*, 23–43. [CrossRef]
99. Righter, K.; Campbell, A.J.; Humayun, M.; Hervig, R.L. Partitioning of Ru, Rh, Pd, Re, Ir, and Au between Cr-bearing spinel, olivine, pyroxene and silicate melts. *Geochim. Cosmochim. Acta* **2004**, *68*, 867–880. [CrossRef]
100. Barnes, S.J.; Maier, W.D. The fractionation of Ni, Cu, and the noble metals in silicate and sulfide liquids. In *Dynamic Processes in Magmatic Ore Deposits and Their Application in Mineral Exploration*; Keay, R.R., Lesher, C.M., Lightfoot, P.C., Farrow, C.E.G., Eds.; Geological Association of Canada: St. John's, NL, Canada, 1999; Volume 13, pp. 69–106.

101. Ruan, B.X.; Liao, M.Y.; Sun, B.K.; Chen, C. Origin and nature of parental magma and sulfide segregation of the Baixintan magmatic Ni-Cu sulfide deposit, southern Central Asian Orogenic Belt (CAOB), NW China: Insights from mineral chemicty of chromite and silicate minerals. *Minerals* **2020**, *10*, 1050. [CrossRef]
102. Zhong, H.; Zhu, W.G.; Chu, Z.Y.; He, D.F.; Song, X.Y. Shrimp U-Pb zircon geochronology, geochemistry, and Nd-Sr isotopic study of contrasting granites in the Emeishan large igneous province, SW China. *Chem. Geol.* **2007**, *236*, 112–133. [CrossRef]
103. Zhou, M.F.; Yang, Z.X.; Song, X.Y.; Lesher, C.M.; Keays, R.R. Magmatic Ni-Cu-(PGE) sulfide deposits in China. In *The Geology, Geochemistry, Mineralogy Mineral Beneficiation of the Platinum-Group Elements*; Cabri, L.J., Ed.; Canadian Institute of Mining, Metallurgy Petroleum: Montreal, QC, Canada, 2002; Volume 54, pp. 619–636.
104. Gao, Z.M.; Zhang, Q.; Tao, Y.; Luo, T.Y. An analysis of mineralization connected with Emeishan mantle plume. *Acta Mineral. Sin.* **2004**, *24*, 99–104. (In Chinese with English abstract)
105. Hu, R.Z.; Tao, Y.; Zhong, H.; Huang, Z.L.; Zhang, Z.W. Mineralization systems of a mantle plume: A case study from the Emeishan igneous province, southwest China. *Earth Sci. Front.* **2005**, *12*, 42–54. (In Chinese with English abstract)
106. Tao, Y.; Hu, R.Z.; Wang, X.Z.; Zhu, D.; Song, X.Y.; Feng, J.Y. The Cu-Ni-PGE mineralization in the Emeishan Large Igneous Province geochemical study on some typical deposits. *Bull. Mineral. Petrol. Geochem.* **2006**, *25*, 236–244. (In Chinese with English abstract)
107. Tao, Y.; Li, C.S.; Hu, R.Z.; Qi, L.; Qu, W.J.; Du, A.D. Re-Os isotopic constraints on the genesis of the Limahe Ni-Cu deposit in the Emeishan large igneous province, SW China. *Lithos* **2010**, *119*, 137–146. [CrossRef]
108. Tang, Q.Y.; Zhang, M.J.; Yu, M.; Wang, Q.L.; Shang, H. The magmatic ore-forming system of late-Permian Emeishan mantle plume. *Acta Petrol. Et Mineral.* **2013**, *32*, 680–692. (In Chinese with English abstract)
109. Tang, Q.Y.; Li, C.S.; Tao, Y.; Ripley, E.M.; Xiong, F. Association of Mg-rich Olivine with magnetite as a result of brucite marble assimilation by basaltic magma in the Emeishan Large Igneous Province, SW China. *J. Petrol.* **2017**, *58*, 699–714. [CrossRef]
110. Shellnutt, J.G. The Emeishan large igneous province: A synthesis. *Geosci. Front.* **2014**, *5*, 369–394. [CrossRef]
111. You, M.X.; Zhang, Z.W.; Liu, J.M.; Zhang, J.W.; Wang, Y.L.; Qian, B. Geochemistry of mafic-ultramafic intrusions and Cu-Ni-(PGE) sulfide deposits in Panxi region, China. *Northwestern Geol.* **2017**, *50*, 146–161. (In Chinese with English abstract)
112. Irvine, T.N. *Petrology of the Duke Island Ultramafic Complex, Southeastern Alaska*; Geological Society of America Memoir: Boulder, CO, USA, 1974; Volume 138, p. 240.
113. Himmelberg, G.R.; Loney, R.A.; Craig, J.T. *Petrogenesis of the Ultramafic Complex at the Blashke Islands, Southeastern Alaska*; U.S. Geological Survey Bulletin; U.S. Government Publishing Office: Washington, DC, USA, 1986; pp. 1–14.
114. Thakurta, J.; Ripley, E.M.; Li, C.S. Oxygen isotopic variability associated with multiple stages of serpentinization, Duke Island Complex, southeastern Alaska. *Geochinica Et Cosmochim. Acta* **2009**, *73*, 6298–6312. [CrossRef]
115. Li, C.S.; Ripley, E.M.; Thakurta, J.; Stifter, E.C.; Qi, L. Variations of olivine Fo-Ni contents and highly chalcophile element abundances in arc ultramafic cumulates, southern Alaska. *Chem. Geol.* **2013**, *351*, 15–28. [CrossRef]
116. Zhang, K.W.; Shen, B.M.; Li, D.Z.; Zhang, Q. The petrochemical characteristics of the Alaskan-type ultramafic rocks. *Geol. Rev.* **1988**, *34*, 377–382. (In Chinese)
117. Barnes, S.J.; Roeder, P.L. The range of spinel compositions in terrestrial mafic and ultramafic rocks. *J. Petrol.* **2001**, *42*, 2279–2302. [CrossRef]
118. Ren, M. Study on petrography, mineralogy and genesis of Baixintan Cu-Ni sulfide deposits in Xinjiang. Master's Thesis, Chang' an University, Xi'an, China, 2017. (In Chinese with English abstract).
119. Feng, Y.Q.; Qian, Z.Z.; Xu, G.; Duan, J.; Chen, B.L.; Sun, T.; Jiang, C.; Ren, M. Rock-forming mineral features of Permian mineralized mafic-ultramafic intrusions in East Tianshan Mountains and their implications for intrusion generation. *Acta Petrol. Et Mineral.* **2017**, *36*, 519–534. (In Chinese with English abstract)
120. Tao, Y.; Li, C.S.; Song, X.Y.; Ripley, E.M. Mineralogical, Petrological, and geochemical studies of the Limahe mafic-ultramafic intrusion and associated Ni-Cu sulfide ores, SW China. *Min. Depos.* **2008**, *43*, 849–872. [CrossRef]
121. Pearce, J.A.; Stern, R.J.; Bloomer, S.H.; Fryer, P. Geochemical mapping of the Mariana arc-basin system: Implications for the nature and distribution of subduction components. *Geochem. Geophys. Geosystems* **2005**, *6*, 1–27. [CrossRef]
122. Campbell, I.H. Identification of ancient mantle plumes. In *Mantle Plumes: Their Identification Through Times*; Special Paper; Ernst, R.E., Buchan, K.L., Eds.; Geological Society of America: Boulder, CO, USA, 2001; Volume 352, pp. 5–21.
123. Ernst, R.E.; Buchan, K.L.; Campbell, I.H. Frontiers in large igenous province research. *Lithos* **2005**, *79*, 271–297. [CrossRef]
124. Xia, L.Q. The geochemical criteria to distinguish continental basalts from arc related ones. *Earth Sci. Rev.* **2014**, *139*, 195–212. [CrossRef]
125. Wang, Y.L.; Zhang, Z.W.; You, M.X.; Li, X.; Li, K.; Wang, B.L. Chronological and characteristics of the Baixintan Ni-Cu deposit in Eastern Tianshan Mountains, Xinjiang, and their implications for Ni-Cu mineralization. *Geol. China* **2015**, *42*, 452–467. (In Chinese with English abstract)
126. Woodhead, J.D.; Hergt, J.M.; Davidson, J.P.; Eggins, S.M. Hafnium isotope evidence for 'conservative' element mobility during subduction zone processes. *Earth Planet. Sci. Lett.* **2001**, *192*, 331–346. [CrossRef]
127. Yang, S.F.; Chen, H.L.; Dong, C.W.; Zhao, D.D. Geochemical properties of late Sinian basalt in the northwestern boundary of Tarim basin and its tectonic setting. *J. Zhejiang Univ.* **1998**, *32*, 753–760. (In Chinese with English abstract)
128. Yu, X.; Chen, H.L.; Yang, S.F.; Li, Z.L.; Wang, Q.H.; Lin, X.B.; Xu, Y.; Luo, J.C. Geochemical features of Permian basalts in Tarim Basin and compared with Emeishan LIP. *Acta Petrol. Sin.* **2009**, *25*, 1492–1498. (In Chinese with English abstract)

129. Jiang, C.Y.; Cheng, S.L.; Ye, S.F.; Xia, M.Z.; Jiang, H.B.; Dai, Y.C. Lithogeochemistry and petrogenesis of Zhongposhanbei mafic rock body, at Beishan region, Xinjiang. *Acta Petrol. Sin.* **2006**, *22*, 115–126. (In Chinese with English abstract)
130. Su, B.X.; Qin, K.Z.; Sun, H.; Tang, D.M.; Xiao, Q.H.; Cao, M.J. Petrological and mineralogical characteristics of Hongshishan complex in Beishan area, Xinjiang: Implications for assimilation and fractional crystallization. *Acta Petrol. Sin.* **2009**, *25*, 873–887. (In Chinese with English abstract)
131. Saccani, E. A new method of discriminating different types of post-Archean ophiolitic basalts and their tectonic significance using Th-Nb and Ce-Dy-Yb systematics. *Geosci. Front.* **2015**, *6*, 481–501. [CrossRef]
132. Wei, X.; Xu, Y.G. Petrogenesis of the mafic dykes from Bachu and implications for the magma evolution of the Tarim large igneous province, NW China. *Acta Petrol. Sin.* **2013**, *29*, 3323–3335. (In Chinese with English abstract)
133. Chen, B.Y.; Yu, J.J.; Liu, S.J. Source characteristics and tectonic setting of mafic-ultramafic intrusions in North Xinjiang, NW China: Insights from the petrology and geochemistry of the Lubei mafic-ultramafic intrusion. *Lithos* **2018**, *308*, 329–345. [CrossRef]
134. Zhao, Y.; Xue, C.J.; Zhao, X.B.; Yang, Y.Q.; Ke, J.J. Magmatic Cu-Ni sulfide mineralization of the Huangshannan mafic-ultramafic intrusion, Eastern Tianshan, China. *J. Asian Earth Sci.* **2015**, *105*, 155–172. [CrossRef]
135. Sun, T.; Qian, Z.Z.; Tang, Z.L.; Jiang, C.Y.; He, K.; Sun, Y.L.; Wang, J.Z.; Xia, M.Z. Zircon U-Pb chronology, platinum group element geochemistry characteristics of Hulu Cu-Ni deposit, East Xinjiang, and its geological significance. *Acta Petrol. Sin.* **2010**, *26*, 3339–3349. (In Chinese with English abstract)
136. Su, B.X.; Qin, K.Z.; Sun, H.; Wang, H. Geochronological, petrological, mineralogical and geochemical studies of the Xuanwoling mafic-ultramafic intrusion in Beishan area, Xinjiang. *Acta Petrol. Sin.* **2010**, *26*, 3283–3294. (In Chinese with English abstract)
137. Ao, S.J.; Xiao, W.J.; Han, C.M.; Mao, Q.G.; Zhang, J.E. Geochronology and geochemistry of Early Permian mafic-ultramafic complexes in the Beishan area, Xinjiang, NW China: Implications for late Paleozoic tectonic evolution of the southern Altaids. *Gondwana Res.* **2010**, *18*, 466–478. [CrossRef]
138. Han, C.M.; Xiao, W.J.; Zhao, G.C.; Su, B.X.; Ao, S.J.; Zhang, J.E.; Wan, B. Age and tectonic setting of magmatic sulfide Cu-Ni mineralization in the Eastern Tianshan Orogenic Belt, Xinjiang, Central Asia. *J. Geosci.* **2013**, *58*, 233–250. [CrossRef]
139. Li, H.Q.; Chen, F.; Mei, Y.; Wu, H.; Cheng, S.; Yang, J.; Dai, Y. Isotopic ages of No. 1 intrusive body in Pobei mafic-ultramafic belt of Xinjiang and their geological significance. *Miner. Depos. Beijing* **2006**, *25*, 463–469. (In Chinese with English abstract)
140. Pearce, J.A. Geochemical fingerprinting of oceanic basalts with applications to ophiolite classification and the search for Archean oceanic crust. *Lithos* **2008**, *100*, 14–48. [CrossRef]
141. Pearce, J.A.; Lippard, S.J.; Roberts, S. Characteristics and tectonic significance of supra-subduction zone ophiolites. In *Marginal Basin Geology*; Kokelaal, B.P., Howells, M.F., Eds.; Special Publications; Geological Society: London, UK, 1984; Volume 16, pp. 77–94.
142. Choe, W.H.; Lee, M.J.; Do, H.S.; Jin, Y.K. Origin of E-MORB in a fossil spreading center: The Antarctic-Phoenix Ridge, Drake Passage, Antarctica. *Geosci. J.* **2007**, *11*, 185–199. [CrossRef]
143. Niu, Y.L.; Liu, Y.; Xue, Q.Q.; Shao, F.L.; Chen, S.; Duan, M.; Guo, P.Y.; Gong, H.M.; Hu, Y.; Hu, Z.X.; et al. Exotic origin of the Chinese continental shelf: New insights into the tectonic evolution of the western Pacific and eastern China since the Mesozoic. *Sci. Bull.* **2015**, *60*, 1598–1616. [CrossRef]
144. Sun, S.S.; Tatsumoto, M.; Schilling, J.G. Mantle plume mixing along the Reykjanes ridge axis: Lead isotopic evidence. *Science* **1975**, *190*, 143–147. [CrossRef]
145. Schilling, J.G.; Zajac, M.; Evans, R.; Johnston, T.; White, W.; Devine, J.D.; Kingsley, R. Petrologic and geochemical variations along the Mid-Atlantic ridge from 29 Degrees N to 73 Degrees, N. *Am. J. Sci.* **1983**, *283*, 510–586. [CrossRef]
146. Bougault, H.; Dmitriev, L.; Schilling, J.G.; Sobolev, A.; Joron, J.L.; Needham, H.D. Mantle heterogeneity from trace elements: MAR triple junction near 14°N. *Earth Planet. Sci. Lett.* **1988**, *88*, 27–36. [CrossRef]